Physics of Fluids

# Diameter ratio effects in the wake flow of single step cylinders

Cite as: Phys. Fluids **32**, 093603 (2020); https://doi.org/10.1063/5.0015378
Submitted: 28 May 2020 . Accepted: 09 August 2020 . Published Online: 02 September 2020

Cai Tian, Fengjian Jiang, Bjørnar Pettersen, Helge I. Andersson, et al.

Physics of Fluids ARTICLE scitation.org/journal/phf

# Diameter ratio effects in the wake flow of single step cylinders

Cite as: Phys. Fluids 32, 093603 (2020); doi: 10.1063/5.0015378
Submitted: 28 May 2020 • Accepted: 9 August 2020 •
Published Online: 2 September 2020



Cai Tian,[1] Fengjian Jiang,[2,a)] Bjørnar Pettersen,[1] and Helge I. Andersson[3]

## AFFILIATIONS

[1]Department of Marine Technology, Norwegian University of Science and Technology (NTNU), NO-7491 Trondheim, Norway
[2]SINTEF Ocean, NO-7052 Trondheim, Norway
[3]Department of Energy and Process Engineering, NTNU, NO-7491 Trondheim, Norway

[a)]**Author to whom correspondence should be addressed:** fengjian.jiang@sintef.no

## ABSTRACT

Vortex interactions behind step cylinders with diameter ratio $2 \le D/d \le 3$ at Reynolds number ($Re_D$) 150 were investigated by directly solving the three-dimensional Navier–Stokes equations. In accordance with the previous paper [C. Tian *et al.*, "Vortex dislocation mechanisms in the near wake of a step cylinder," J. Fluid Mech. **891**, A24 (2020)], some interesting characteristics of vortex dislocations, e.g., two phase difference accumulation mechanisms, the trigger and threshold values of vortex dislocations, antisymmetric vortex interactions, and long N-cell cycles, were observed. By performing a detailed investigation of diameter ratio effects, more features of vortex dynamics were discovered. In addition to the known antisymmetric vortex interactions, a symmetric vortex interaction between neighboring N-cell cycles was observed. The long-time observations revealed an interruption of these two types of vortex interactions. By using a well-validated phase tracking method, we monitored the time trace of the phase difference accumulation process in different $D/d$ cases from which decreasing (known) and increasing (new) phase difference tendencies were identified. Both caused the interruption of continuous symmetric or antisymmetric phenomena but through two distinct mechanisms. Meanwhile, the diameter ratio effects on the trigger and threshold values were discussed. Additionally, the likelihood of antisymmetric or symmetric vortex interactions and increasing or decreasing phase difference tendencies was analyzed. Moreover, diameter ratio effects on shedding frequencies and the extensions of three main vortex cells, i.e., S-, N-, and L-cell vortices, were described.



## I. INTRODUCTION

In recent years, fluid flow around a step cylinder configuration, as shown in Fig. 1, has been the focus of many studies. Flow past structures with a similar shape occurs in many engineering applications, for example, the outer wall of TV-towers, the underwater hull of a SPAR-buoy, and the supporting structures for fixed and floating offshore wind turbines. For a sufficiently long single step cylinder, there are mainly two important parameters, i.e., the diameter ratio ($D/d$) and the Reynolds number ($Re_D$). $D/d$ is the diameter ratio between the large- and small-part of the step cylinder, while $Re_D = UD/\nu$ (where $\nu$ is the kinematic viscosity of the fluid and $U$ represents the uniform inflow velocity).

Based on experimental investigations in the wake of a step cylinder with $D/d \approx 2$ at $63 < Re_D < 1100$, Dunn and Tavoularis[1] identified three types of spanwise vortices: (1) S-cell vortex shed from the small cylinder with the highest shedding frequency $f_S$, (2) L-cell vortex shed from the large cylinder with shedding frequency $f_L$, and (3) N-cell vortex located between the S- and L-cell vortices with the lowest shedding frequency $f_N$. Lewis and Gharib[2] found that the N-cell vortex (the modulation zone) only exists when $D/d > 1.55$, where there is no direct connection between the S- and L-cell vortices. They called it the *indirect mode*. Meanwhile, a *direct mode* was identified when $D/d < 1.25$, where the N-cell vortex disappears and the corresponding S- and L-cell vortices directly connect to each other.

The N-cell vortex has the lowest shedding frequency among the three dominating vortex cells, i.e., the S-, N-, and L-cell vortices. Similar low-frequency cells were also observed in the wake behind several other configurations, e.g., the wake behind a free-end cylinder,[3] the wake behind a circular cylinder with flat end-plates,[4] and the wake behind a concave curved cylinder.[5] The previous

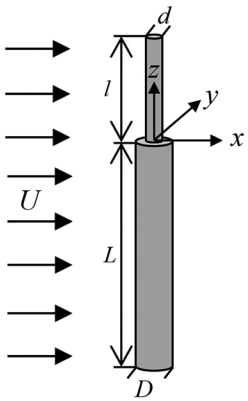


**FIG. 1**. A sketch of the step cylinder geometry. The diameters of the small and large cylinders are *d* and *D*, respectively. *l* is the length of the small cylinder, and *L* is the length of the large cylinder. The origin locates at the center of the interface between the small and large cylinders. The uniform incoming flow *U* is in the positive *x*-direction. The three directions are named streamwise (*x*-direction), crossflow (*y*-direction), and spanwise (*z*-direction).

studies[1,4,6,7] attributed the appearances of such low-frequency cells (N-cell-like vortex) to 3D effects, which include mainly two mechanisms: downwash and increased base pressure. Bearman[8] and Williamson[4] found that the increased base pressure has the effect of increasing the vortex formation region and causes the vortex shedding frequency to decrease. Zdravkovich *et al.*[6] and Williamson[4] found that the spanwise velocity (downwash) could not merely displace the vortex formation region further downstream but also widen the separated shear layers before they roll up into vortices. These effects would also decrease the vortex shedding frequency. For the wake behind the step cylinder, by doing experiments and numerical simulations, Dunn and Tavoularis[1] and Morton *et al.*[7] also concluded that the 3D effect is a plausible explanation of the formation of the N-cell vortex. However, there is no further discussion about the relative importance of these two 3D effects, i.e., the downwash and the increased base pressure. In Sec. III B 1, their relative importance will be discussed.

Whenever there are several spanwise-oriented vortex cells with different frequencies, these vortices are either in phase or out of phase with each other. As they move out of phase, a contorted "tangle" of vortices appears at the boundary between them, which looks like dislocations that appear in solid materials. Williamson[4] defined this kind of flow phenomenon as *vortex dislocation*. By doing experiments of flow past a circular cylinder with end-plates at $Re_D < 200$, Williamson found that the vortex dislocation occurs at the boundary between the central vortex cell of frequency $f_u$ and the single vortex cell of frequency $f_l$ at a beat frequency $f_u - f_l$. Between two neighboring vortex dislocations, he proposed to estimate the number of vortex shedding cycles of the central vortex cell ($n_u$) and the single vortex cell ($n_l$)[4] as

$$n_u = f_u/(f_u - f_l), \tag{1}$$

$$n_l = n_u - 1. \tag{2}$$

In the wake of a step cylinder, the vortex dislocations between S-, N-, and L-cell vortices were also the topic of many investigations.[1,2,7,9–12] All these studies concluded that the interactions between the S- and N-cell vortices occur in a narrow S–N cell boundary (the region between the S- and N-cell vortices), which is stable and deflects spanwise into the large cylinder region. During the dislocation process, the N-cell vortex splits into at least two filaments. One of these filaments connects to the subsequent N-cell vortex of the opposite sign to form a hairpin-like vortex structure. The other filament connects to the S-cell vortex.[1,11–13] Except for the S-cell vortices that connect to the N-cell vortices, the rest of them form S–S half loops,[11] which appear at a beat frequency ($f_S - f_N$).

Unlike the S–N cell boundary, the N–L cell boundary (the region between the N- and L-cell vortices) is relatively wide and varies with time. Lewis and Gharib[2] first observed an inclined interface region (the N–L cell boundary) appearing behind the large cylinder at beat frequency ($f_L - f_N$). Morton and Yarusevych[11] explained this phenomenon: as the phase difference between the N- and L-cell vortices accumulates, accompanying with the appearance of vortex dislocations between N- and L-cell vortices, the shapes and lengths of the N-cell vortices and the position of the N–L cell boundary periodically change at the beat frequency ($f_L - f_N$). They defined these cyclic variations as the N-cell cycle.[11] More detailed vortex interactions in the N-cell cycles were investigated by Tian *et al.*[14–17] They observed that in the wake behind a single step cylinder ($D/d = 2$) at $Re_D = 150$, there are two NL-loops (NL-loop 1 and NL-loop 2), one NN-loop and at least one LL-half-loop structure in one N-cell cycle. The phrase *antisymmetric vortex interaction* was introduced to describe the phenomenon that the NL-loop structures form at different sides of the step cylinder in the neighboring N-cell cycles. Moreover, Tian *et al.*[17] reported that the total phase difference, Φ, is accumulated by the joint influence of different shedding frequencies and different convective velocities. This mechanism was described as

$$\Phi = \Phi_f + \Phi_c, \tag{3}$$

where $\Phi_f$ and $\Phi_c$ represent the Φ caused by different shedding frequencies and different convective velocities, respectively. By tracking the phase information on N- and L-cell vortices, they measured $\Phi_f$ of every N–L vortex pair,

$$\Phi_f = \varphi_N - \varphi_L. \tag{4}$$

Here, $\varphi_N$ and $\varphi_L$ represent the phase information on the corresponding N- and L-cell vortices, respectively. By plotting the long-time trace of the accumulation of $\Phi_f$, a decreasing tendency of $\Phi_f$ was observed by Tian *et al.*,[17] which makes the formation position of the corresponding NL-loop structure move downstream in subsequent N-cell cycles and finally causes an interruption of the continuous antisymmetric vortex interactions. An uninterrupted series of antisymmetric N-cell cycles was identified as the long N-cell cycle. The gradual decrease in $\Phi_f$ can be evaluated as

$$S = \alpha\frac{1}{2f_L} - \beta\frac{1}{2f_N}, \tag{5}$$

where $S$ (with dimension $D/U$) is a measure of the phase shift of the N–L vortex pair in one N-cell cycle, as compared to the corresponding N–L vortex pair in the previous N-cell cycle. In this expression,

$\alpha$ and $\beta$ are the number of L- and N-cell vortices in one N-cell cycle, respectively. Tian *et al.*[17] found that only when $\Phi_f$ becomes larger than a certain value (referred to as the *threshold value*), taking $\Phi_c$ into account, $\Phi$ can be sufficiently large (referred to as the *trigger value*) to induce the vortex dislocation and the formation of the NL-loops.

In previous papers,[1,11,13,18] vortex interactions between S- and N-cell vortices were described in detail. The primary goal of the present numerical study is to investigate the effects of the diameter ratio ($D/d$) on the vortex interactions, especially the vortex dislocations between N- and L-cell vortices in the wake behind the step cylinder. As shown by Morton and Yarusevych,[11] when $Re_D$ increases to 300, many small streamwise vortices appear. To prevent these vortices from disturbing the observations of vortex interactions, we choose to stay at $Re_D$ = 150 to demonstrate the detailed vortex connections more clearly. To achieve this, we analyze the space and time signals of several flow quantities (velocity, vorticity, and $\lambda_2$[19]) obtained from a direct numerical simulation (DNS) of flow past 10 different step cylinders with diameter ratios $D/d$ = 2.0, 2.1, 2.2, 2.3, 2.4, 2.5, 2.6, 2.7, 2.8, and 3.0. All these cases share the same coordinate system, grid resolution, and computational method. By using a well validated phase difference tracking method,[17] the phase difference accumulation process is further investigated.

All discussions in Secs. II–IV are based on the $D/d$ = 2.0, 2.2, 2.4, 2.6, 2.8, and 3.0 cases. In Sec. II, the flow problem and the numerical settings are introduced. Then, the wake and the diameter ratio effects on the three main vortex cells, i.e., the S-, N-, and L-cell vortices, are described in Sec. III. In Sec. IV, the diameter ratio effects on the vortex dislocations between N- and L-cell vortices are discussed in detail, and additional characteristics of the vortex dislocations are revealed. In Sec. V, we analyze the likelihood of different characteristics of vortex dislocations. The $D/d$ = 2.1, 2.3, 2.5, and 2.7 cases are investigated to further support our discussions and strengthen our conclusions.

## II. FLOW CONFIGURATION AND COMPUTATIONAL ASPECTS

### A. Flow configuration and coordinate system

The step cylinder investigated in the present paper is illustrated in Fig. 1. The uniform incoming flow $U$ is in the positive $x$-direction. In Fig. 2, a side view and a top-down view of the flow domain are shown. The height of the domain is 45$D$ of which the small and large cylinders occupy 15$D$ ($l$) and 30$D$ ($L$), respectively. The inlet boundary locates at 10$D$ upstream from the origin, and the outlet boundary locates at 20$D$ downstream. The width of the domain is 20$D$. This domain size is comparable to, or exceeds, that used in previous similar studies.[11,15,17] Most of the results in the present paper are from the six cases $D/d$ = 2.0, 2.2, 2.4, 2.6, 2.8, and 3.0. In order to keep the Reynolds number of the large cylinder ($Re_D$) at 150 in all cases, we keep $D$ constant and change $d$. Boundary conditions used in the present study are as follows:

- The inlet boundary: uniform velocity profile $u = U$, $v = 0$, and $w = 0$.
- The outlet boundary: Neumann boundary condition for velocity components ($\partial u/\partial x = \partial v/\partial x = \partial w/\partial x = 0$) and constant zero pressure condition.

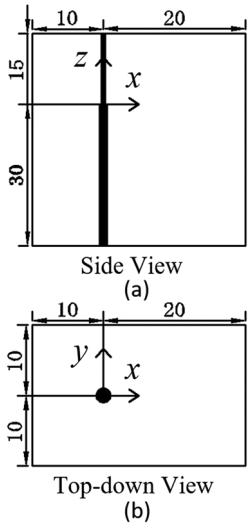


**FIG. 2**. Computational domain, origin, and coordinate system are illustrated from (a) side view and (b) top-down view. The diameter of the large cylinder, $D$, is the length unit. The origin is located in the center of the step at the interface between the small and large cylinders.

- The other four sides of the computational domain: free-slip boundary conditions for the two vertical sides ($v = 0$ and $\partial u/\partial y = \partial w/\partial y = 0$) and for the two horizontal sides ($w = 0$ and $\partial u/\partial z = \partial v/\partial z = 0$).
- The step cylinder surfaces: no-slip and impermeable wall.

### B. Computational method

The three-dimensional time-dependent incompressible Navier–Stokes equations are directly solved by a well-verified finite-volume based numerical code *MGLET*.[20] The surface integral of flow variables over the faces of the discrete volumes is approximated by using the midpoint rule, which leads to second-order accuracy in space. The discretized equations are integrated in time with a third-order explicit low-storage Runge–Kutta scheme.[21] A constant time step $\Delta t$ is used to ensure a CFL number smaller than 0.65. The pressure corrections are handled by solving a Poisson equation with Stone's implicit procedure (SIP).[22] The same code has recently been used to investigate other flows around three-dimensional bluff bodies, such as the step cylinder wake,[17] the spheroid wake,[23] and the curved cylinder wake.[5]

In all simulations, an immersed boundary method (IBM) is used to handle the cylindrical geometry inside the Cartesian grid. The details of this IBM and its validation can be found in Ref. 24. The overall properties of the grids for all cases are shown in Table I. A schematic illustration of the mesh design can be found in Fig. 3 of Ref. 17. First, the computational domain is divided into equal-sized cubic Cartesian grid boxes, named the level-1 grid. Each grid box is further equally divided into $N \times N \times N$ cubic grid cells. In the regions where complex flow phenomena take place, e.g., the regions close to the step cylinder geometry and the regions where vortex dislocations happen, the grid boxes (the level-1 box) are equally split into

**TABLE I**. Detailed mesh information. The Reynolds number is $Re_D = UD/\nu = 150$. Mesh A is used in all cases. Mesh B is only used in the $D/d = 2.8$ case for the grid convergence test.

| Mesh | Minimum grid cell size, $\Delta/D$ | Time step, $\Delta tU/D$ | Number of grid levels | Number of grid cells in one grid box | Total number of grid cells (million) |
|---|---|---|---|---|---|
| A | 0.015 | 0.005 | 6 | $24 \times 24 \times 24$ | 124.1 |
| B | 0.012 | 0.004 | 6 | $30 \times 30 \times 30$ | 243.3 |

eight smaller cubic grid boxes (the level-2 grid box). There are also $N \times N \times N$ cubic grid cells in every level-2 grid box. Therefore, the grid resolution in the level-2 grid box is two times finer than that in the level-1 grid box. This refinement-process continuously goes on until a sufficient grid resolution is reached. More detailed information on this local grid refinement method can be found in Ref. 20.

### C. Grid convergence

A detailed grid convergence study can be found in our previous paper,[17] which proves that in the $D/d = 2.0$ case, the minimum grid cell size $\Delta/D = 0.015$ is fine enough to resolve all physical phenomena of interest to us. We note that $\Delta$ is normalized by $D$, therefore, close to the small cylinder surface, the grid resolution may be challenged. As we cover different $D/d$ cases in the present study, the grid resolution for a small cylinder needs to be addressed. When $D/d = 3$, the Reynolds number for the small cylinder ($Re_d$) is 50, which is very close to the $Re$ range of the closed wake regime ($4–5 \le \mathrm{Re} \le 30–48$). In this $Re$ range, there is no periodic vortex shedding behind the cylinder. Considering that both the vortex shedding and the abrupt change in diameter complicate the flow, the major challenge to the local grid resolution around the small cylinder should appear when $D/d = 2.8$ ($Re_d = 53$). The grid size in the $D/d = 2.8$ case is further refined from $\Delta/D = 0.015$ (mesh A) to 0.012 (mesh B) to check the grid convergence, as shown in Table I. In Fig. 3(a), the distributions of time-averaged streamwise velocity along the vertical line AB [as indicated in Fig. 3(b)] for these two $D/d = 2.8$ cases are plotted to

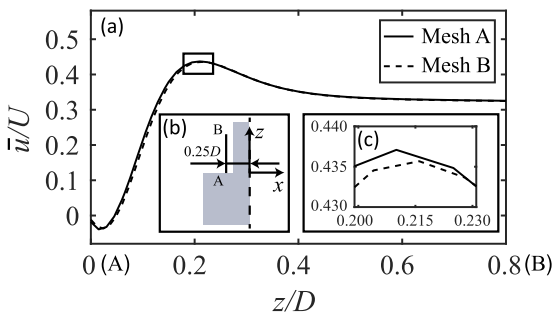


**FIG. 3**. (a) Distributions of time-averaged streamwise velocity $\overline{u}/U$ along a sampling line AB in the $x$–$z$ plane at $y/D = 0$ in the $D/d = 2.8$ case. Inset: (b) a sketch of the position of the sampling line AB of length 0.8D at $x/D = -0.25$ and (c) a zoomed-in view of the upper part of the curves (black rectangle) in panel (a).

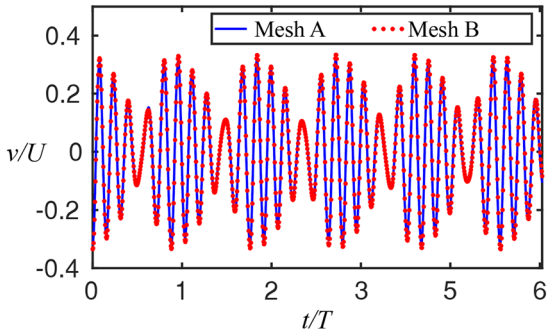


**FIG. 4**. Time traces of the crossflow velocity $v$ at point ($x/D$, $y/D$, $z/D$) = (1, 0, −6) in the $D/d = 2.8$ case by using mesh A and mesh B. $T$ is the period of one N-cell cycle.

illustrate the flow variation on the "step" in front of the small cylinder. As shown in Figs. 3(a) and 3(c), only tiny differences appear when the grid size is refined. Moreover, Fig. 4 shows the time traces of the crossflow velocity ($v$) in the interaction region between the N- and L-cell vortices where the velocity varies dramatically with time due to the vortex dislocations. The fluctuations and the mean values of $v$ from mesh A and mesh B almost coincide. However, the computational cost of mesh B is significantly higher than that of mesh A due to the large number of grid cells and smaller time step. All discussions are therefore based on grid resolution $\Delta/D = 0.015$. To ensure that the flow is properly developed, all cases were simulated first for at least 300 time units ($D/U$) and then continued for at least $2000D/U$ to collect the statistical data.

## III. DIAMETER RATIO EFFECTS ON THE SHEDDING FREQUENCIES AND THE EXTENSIONS OF VORTEX CELLS

### A. Diameter ratio effects on the S-cell vortex

The diameter ratio $D/d$ dramatically changes the wake and influences each vortex cell. This is indicated in Fig. 5, where the approximate extensions of the S-, N-, and L-cell vortices are marked. From Figs. 5(a)–5(c), one obvious change is the absence of the S-cell vortices in Fig. 5(c), i.e., the $D/d = 3.0$ case. As mentioned in Sec. II, when $D/d$ increases from 2 to 3, the Reynolds number of the small cylinder ($Re_d$) decreases from 75 to 50, which is at the border between the steady separation regime ($4–5 < Re < 30–48$) and the periodic laminar regime[27] ($30–48 < Re < 180–200$). Considering the disturbance caused by the vortex shedding behind the large cylinder, we expected vortex shedding to be triggered also behind the small cylinder. However, no vortex shedding can be observed there. As shown in the second column in Table II, $St_S$ gradually increases as $D/d$ increases. As a result, there is one more S-cell vortex behind the small cylinder ($D/d = 2.4$) in Fig. 5(b) than in the $D/d = 2.0$ case in Fig. 5(a). Comparing with the empirical $St'_S$ in the sixth column of Table II, the maximum difference between $St_S$ and $St'_S$ is only 3.2%. The variation in $St_S$ is simply caused by changes in $Re_d$, i.e., clearly $D/d$ dependent. In Fig. 6, the extensions of the three vortex cells (the S-, N-, and L-cell vortices) are shown. To find it, the

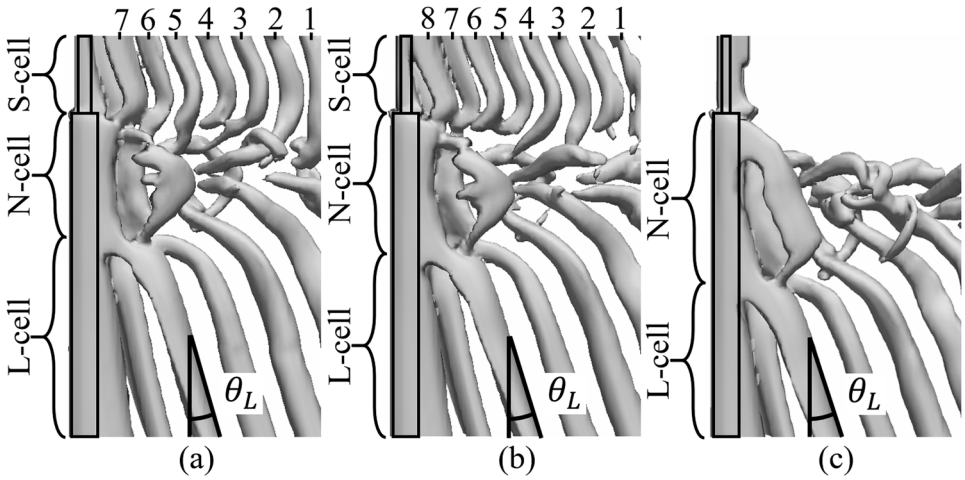


**FIG. 5**. Instantaneous isosurface of $\lambda_2 = -0.05$ at $Re_D = 150$: (a) the $D/d = 2.0$ case, (b) the $D/d = 2.4$ case, and (c) the $D/d = 3.0$ case. The approximate extensions of the three vortex cells (S-, N-, and L-cell vortices) and the oblique shedding angle $\theta_L$ of the L-cell vortices are indicated. The S-cell vortices in (a) and (b) are labeled by serial numbers. Note: the S-cell vortices disappear in (c) due to $Re_d = 50$ in the $D/d = 3.0$ case. $\lambda_2 = -0.05$ is selected to be consistent with the value of $\lambda_2$ used in Refs. 15 and 17. The choice of the $\lambda_2$ value affects only the size of the vortex tubes but not their number.

**TABLE II**. Detailed information on the S-, N-, and L-cell vortices in six cases. In the second, third, and fourth columns, Strouhal numbers of these three dominating vortex cells ($St_S = f_S D/U$, $St_N = f_N D/U$, and $St_L = f_L D/U$) are shown. They are obtained by means of a discrete Fourier transform (DFT) of continuous velocity data along a vertical sampling line with density $0.2D$ parallel to the $z$-axis at position $(x/D, y/D) = (1.6, 0.4)$, over at least 2000 time units ($D/U$). In the fifth column, $\Delta_{NL}$ is calculated by $(St_L - St_N)/St_L$. $\theta_L$ is the oblique shedding angle of the L-cell vortices, as shown in Fig. 5. In the sixth column, the empirical Strouhal number of the small cylinder ($St'_S$) is calculated as $St'_S = (0.2663 - 1.019/Re_d^{0.5}) \times 2$ from Ref. 25. By means of the Williamson and Brown[26] correlation, $St_{L\theta} = (0.2731 - 1.1129/Re_D^{0.5} + 0.4821/Re_D) \times \cos(\theta_L)$, the empirical Strouhal number of the large cylinder ($St_{L\theta}$) is calculated and shown in the eighth column. Note: the frequency resolution in this table is between $0.0004U/D$ and $0.0005U/D$. A higher frequency resolution may lead to some minor differences in the characteristic frequency in this table. These differences are however small and do not affect our discussions and conclusions.

| $D/d$ | $St_S$ | $St_N$ | $St_L$ | $\Delta_{NL}$ (%) | $St'_S$ | $\theta_L$ (deg) | $St_{L\theta}$ |
|---|---|---|---|---|---|---|---|
| 2.0 | 0.2895 | 0.1545 | 0.1780 | 13.2 | 0.2972 | 16 | 0.1776 |
| 2.2 | 0.3084 | 0.1516 | 0.1775 | 14.6 | 0.3142 | 17 | 0.1773 |
| 2.4 | 0.3221 | 0.1501 | 0.1771 | 15.2 | 0.3297 | 17 | 0.1773 |
| 2.6 | 0.3350 | 0.1491 | 0.1768 | 15.7 | 0.3435 | 18 | 0.1764 |
| 2.8 | 0.3444 | 0.1480 | 0.1765 | 16.1 | 0.3558 | 18 | 0.1764 |
| 3.0 | No-shedding | 0.1464 | 0.1761 | 16.9 | ... | 18 | 0.1764 |

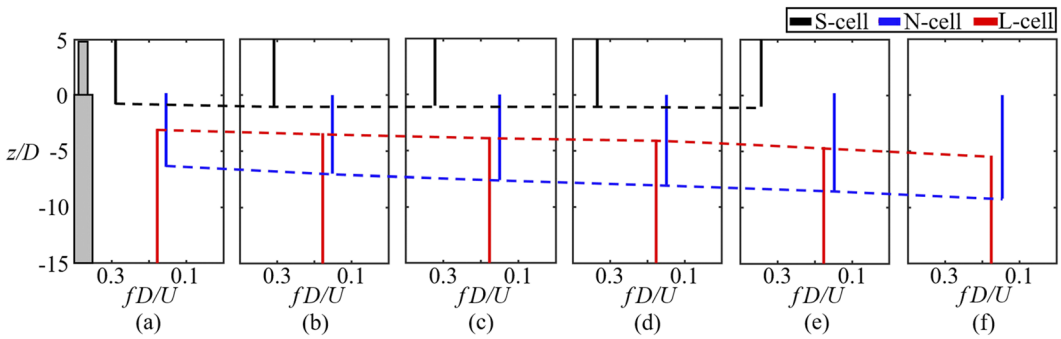


**FIG. 6**. Distributions of dimensionless vortex shedding frequency across the span of the step cylinders at $Re_D = 150$, $D/d = 2.0$, 2.2, 2.4, 2.6, 2.8, and 3.0 cases are plotted in (a)–(f), respectively. By connecting the lower end of the S- and N-cell regions, and the upper end of L-cells, the trend of extensions of these three vortex cells is illustrated by a black, a blue and a red dashed line, respectively.

streamwise velocity spectra for all six cases are calculated along a vertical sampling line parallel to the $z$-axis at position ($x/D$, $y/D$) = (1.6, 0.4). More detailed information about streamwise velocity spectra is shown in Figs. 16–21 in Appendix A. For a given spanwise position, only the spectral peaks with the energy accounting for at least 4% of the total energy in the spectra at this spanwise position are taken into consideration. In Fig. 7 of Ref. 11, the authors used a similar method to identify different vortex cell regions. In Figs. 6(a)–6(e), by connecting the lower end of the S-cell extension, a black dashed curve is plotted to illustrate the variation of the S-cell regions. Except for a very small decrease in Fig. 6(a), i.e., the $D/d$ = 2 case, no obvious change can be observed when $D/d$ increases from 2 [Fig. 6(a)] to 2.8 [Fig. 6(e)]. Generally, in the present low-Reynolds-number step cylinder wakes, the flow behind the small cylinder is seldomly influenced by the abruptly changed diameter at the step position when $2 < D/d < 3$. This agrees well with previous studies.[1,9,17,28]

## B. Diameter ratio effects on the N- and L-cell vortices

### 1. Formation of the N-cell vortex

For the N- and L-cell vortices, the $D/d$ effects are more complicated. Table II and Fig. 5 show that both their shedding frequencies and extensions are influenced. Before taking further steps, we would like to revisit a basic question, i.e., what causes the N-cell vortex. As mentioned in Sec. I, the previous studies[1,11] attributed the appearance of the N-cell vortex to a combination of two 3D effects: downwash and increased base pressure. Both these two 3D effects can increase the vortex formation region and cause the vortex shedding frequency to decrease.[4,6,8] Instead of following the previous studies to further discuss the N-cell vortex formation mechanism, the relative importance of these two 3D effects is discussed in the following.

In Figs. 7(a) and 7(b), the distributions of time-averaged spanwise velocity $-\overline{w}/U$ and the time-averaged base pressure coefficient $\overline{C_{pb}}$ are plotted, respectively. By checking the lower end of N-cell extensions in Fig. 6 (blue dashed line), black circles are added to Fig. 7 to illustrate the end position of the N-cell vortex region. Generally, the results agree well with previous investigations.[1,4,6,7] Clear spanwise velocity (downwash) $-\overline{w}/U$ and increased base pressure $\overline{C_{pb}}$ can be observed in the N-cell region (the part of the curves at the right side of the black circles). As $D/d$ increases, this becomes even more obvious. If $-\overline{w}/U$ is assumed to be the key factor that causes the formation of the N-cell vortex, some paradoxical observations arise. For example, by looking at the distribution of $-\overline{w}/U$ in the $D/d$ = 2.0 case, i.e., the solid blue line in Fig. 7(a), one can see that $-\overline{w}/U$ in the L-cell region ($z/D < -10$) is even larger than that in a part of the N-cell vortex area ($-6.4 < z/D < -6$). In other words, if we assume that it is the strong $-\overline{w}/U$ that induces the formation of the N-cell vortex, the N-cell vortex should extend to the area $z/D < -10$, instead of ending at $z/D = -6.4$ in the $D/d$ = 2.0 case. A similar paradox also appears in the $D/d$ = 2.2, 2.4, and 2.6 cases. On the other hand, as shown in Fig. 7(b), $\overline{C_{pb}}$ in the N-cell region is larger than that outside of the N-cell region for all six cases. In the region $z/D < -10$, $\overline{C_{pb}}$ of the six cases approximately converges to a value around −0.8. In the N-cell region, $\overline{C_{pb}}$ is obviously larger than this. In our opinion, the appearance of the N-cell vortex can be the joint influence of both the spanwise velocity $-\overline{w}/U$ and the increased base pressure $\overline{C_{pb}}$ (the 3D effects). The increased $\overline{C_{pb}}$, however, plays a major role.

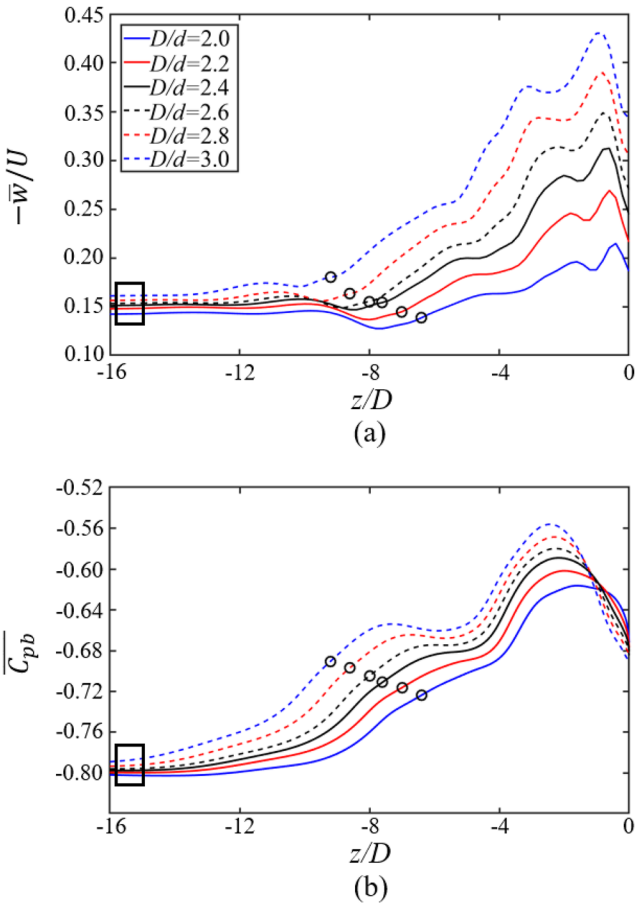


**FIG. 7**. (a) Time-averaged spanwise velocity $-\overline{w}/U$ along a spanwise sampling line at ($x/D$, $y/D$) = (1, 0) in the large cylinder region and (b) time-averaged base pressure coefficient $\overline{C_{pb}}$ measured by $\overline{C_{pb}} = (\overline{P_b} - P_0)/(0.5\rho U^2)$, where $P_0$ is the pressure at the inlet boundary and $\overline{P_b}$ is the time-averaged pressure along a sampling line at ($x/D$, $y/D$) = (0.53, 0) in the large cylinder region. [Note: Due to the way a curved surface is interpreted in the IBM, completely smooth surface pressure distributions are hardly obtained. $\overline{P_b}$ is obtained at ($x/D$, $y/D$) = (0.53, 0), instead of at ($x/D$, $y/D$) = (0.5, 0). The distance $h = 0.03D$ is selected because it is slightly larger than the smallest cell's diagonal ($\sqrt{3}\Delta < h = 0.03D < 1.5\sqrt{3}\Delta$, where $\Delta = 0.015D$) such that we safely avoid wiggles possibly caused by cells directly cut by the cylinder surface and still stay as close as possible to the surface.] The values of $-\overline{w}/U$ and $\overline{C_{pb}}$ in the L-cell region ($z/D = -16$) are shown in the ninth and tenth columns in Table IV.

### 2. Spanwise extensions and shedding frequencies of the N- and L-cell vortices

In Figs. 6(a)–6(e), one can clearly observe two transition regions along the span of the step cylinder: (i) the S–N transition region where both the S- and N-cell vortices may coexist and (ii) the N–L transition region where both the N- and L-cell vortices may coexist. The spanwise ranges of these two transition regions are

**TABLE III**. Spanwise range of the S–N and N–L transition regions.

| $D/d$ | S–N transition region | N–L transition region |
|---|---|---|
| 2.0 | $-0.8 \le z/D \le 0.2$ | $-6.4 \le z/D \le -3.0$ |
| 2.2 | $-1.0 \le z/D \le 0$ | $-7.0 \le z/D \le -3.4$ |
| 2.4 | $-1.0 \le z/D \le 0$ | $-7.6 \le z/D \le -3.8$ |
| 2.6 | $-1.0 \le z/D \le 0$ | $-8.0 \le z/D \le -4.0$ |
| 2.8 | $-1.0 \le z/D \le 0.2$ | $-8.6 \le z/D \le -4.6$ |
| 3.0 | ... | $-9.2 \le z/D \le -5.4$ |

shown in Table III. In agreement with previous observations,[1,2,11] the spanwise length of the S–N transition region is significantly smaller than that of the N–L transition region. In Fig. 7 of Ref. 11, Morton and Yarusevych showed that both the S–N and N–L transition regions keep constant, when $Re_D$ increases from 150 to 300 in the $D/d$ = 2.0 case. In the present paper, we define the center position of the transition region as its location. Table III shows that at $Re_D$ = 150, the changed diameter ratios ($2 \le D/d \le 3$) have a limited effect on the S–N transition region. The position of the S–N transition region shifts 0.2$D$ to the small cylinder side in the $D/d$ = 2.0 case, and the spanwise length of the S–N transition region decreases from 1$D$ to 0.8$D$ in the $D/d$ = 2.8 case. Considering that the frequency analysis is based on data obtained from a sampling line with density (0.2$D$) in the spanwise ($z$) direction, these fluctuations in the S–N transition region can be neglected. On the other hand, the variation in the N–L transition region is obvious. When $D/d$ increases from 2 to 3 [Figs. 6(a)–6(f)], except for a tiny decrease in the $D/d$ = 3 case, the spanwise length of the N–L transition region gradually increases from 3.4$D$ to 4$D$. Meanwhile, the position of the N–L transition region continuously moves to the large cylinder side from $z/D = -4.6D$ to $-7.3D$. As a result, at the large cylinder side, the spanwise extension of the N-cell vortex increases, whereas the spanwise extension of the L-cell vortex decreases. According to discussions in Sec. III B 1, this can be caused by the increased strength and the increased impact area of the 3D effects (i.e., downwash and increased base pressure), as shown in Fig. 7. As the N-cell region continuously expands to the large cylinder side, shrinking of the L-cell region subsequently appears.

The shedding frequencies of both N- and L-cell vortices are affected by the joint influences of the spanwise velocity and the increased $\overline{C_{pb}}$. As mentioned in Sec. I, both the increased $\overline{C_{pb}}$ and $-\overline{w}/U$ can reduce the shedding frequency of the affected vortex. By combining information from Table II and Fig. 7, it is clear that as the base pressure and the strength of the spanwise velocity in the N-cell region increase from the $D/d$ = 2.0 to the $D/d$ = 3.0 case, the corresponding $St_N$ continues to decrease from 0.1545 to 0.1464, a drop of 5.2%. Meanwhile, $St_L$ only drops 1.1%, i.e., from $St_L$ = 0.1780 in the $D/d$ = 2.0 case to $St_L$ = 0.1761 in the $D/d$ = 3.0 case. This is because the N-cell region is closer to the step position than the L-cell region is, which makes $\overline{C_{pb}}$ and $-\overline{w}/U$ in the N-cell region more sensitive to the varying $D/d$. In Fig. 7 and Table IV, when $D/d$ increases from 2 to 3, $\overline{C_{pb}}$ increases around 10% in the N-cell region but only 2% in the L-cell region. Similarly, $-\overline{w}/U$ in the N-cell region doubles from the $D/d$ = 2.0 to $D/d$ = 3.0 case. In the L-cell region, however, the increment is only 15%. The different decline rates of $St_N$ and $St_L$ make their difference ($\Delta_{NL}$) increase from 13.2% to 16.8%, as seen in the fifth column in Table II. We may speculate that $\Delta_{NL}$ will continue to increase if $D/d$ is further increased. For fixed $D$ and $Re_D$, the maximum $\Delta_{NL}$ can be obtained when $D/d$ tends to infinite, i.e., the free end circular cylinder case. In support of this speculation, Ayoub and Karamcheti[3] reported a 23% frequency drop from the main cell to the end cell of a circular cylinder with one free end, which is substantially larger than that in the present study.

## IV. INTERACTIONS BETWEEN THE N- AND L-CELL VORTICES

### A. Variation in phase difference between N- and L-cell vortices

The gradual decrease in phase difference $S$ [Eq. (5)] is an important quantity to characterize vortex dislocations, as discussed in Sec. I. A positive $S$ value and a subsequent decreasing tendency in the time trace of the phase difference were observed in the $D/d$ = 2.0 and 2.4 cases.[16,17] We hypothesized that an increasing tendency may also exist. This is confirmed through more detailed parameter studies in the present paper.

By using the same phase-tracking method introduced by Tian *et al.*,[17] the time traces of $\Phi_f$ between the corresponding N- and L-cell vortices in all six $D/d$ cases are illustrated in Fig. 8. We use green and red circles to indicate $\Phi_f$ of the N–L vortex pairs whose dislocations eventually cause NL-loop 1 and NL-loop 2, respectively. The trends of these two kinds of circles are illustrated by two solid

**TABLE IV**. Detailed information on vortex dislocations in the six present $D/d$ cases. The number of N- and L-cell vortices in one N-cell cycle is $\beta$ and $\alpha$, respectively. The variation rate of phase difference ($S$) is calculated by Eq. (4). In the last two columns, $-\overline{w}/U$ and $\overline{C_{pb}}$ are obtained from Fig. 7 at $z/D = -16$.

| $D/d$ | $\beta$ | $\alpha$ | Symmetry or antisymmetry | $SU/D$ | Tendency of $\Phi_f$ | Threshold value | Trigger value | $-\overline{w}/U$ | $\overline{C_{pb}}$ |
|---|---|---|---|---|---|---|---|---|---|
| 2.0 | 13 | 15 | Antisymmetry | 0.064 | Decrease | 4.3 | 5.5 | 0.1422 | −0.8018 |
| 2.2 | 12 | 14 | Symmetry | −0.153 | Increase | 4.2 | 5.5 | 0.1477 | −0.7992 |
| 2.4 | 11 | 13 | Antisymmetry | 0.094 | Decrease | 4.1 | 5.4 | 0.1511 | −0.7974 |
| 2.6 | 11 | 13 | Antisymmetry | −0.104 | Increase | 3.6 | 5.5 | 0.1531 | −0.7958 |
| 2.8 | 10 | 12 | Symmetry | 0.229 | Decrease | 3.2 | 5.5 | 0.1563 | −0.7932 |
| 3.0 | 10 | 12 | Symmetry | −0.059 | Increase | 3.0 | 5.5 | 0.1611 | −0.7888 |

lines with the corresponding colors. Distinct decreasing and increasing tendencies of $\Phi_f$ can be seen in the left and right parts of Fig. 8, respectively. Moreover, the relation between $S$ and the corresponding tendency of $\Phi_f$ is shown in Table IV, which makes it convincing to conclude that the variation tendency of $\Phi_f$ is directly associated with the sign of $S$. This relationship can be explained by some mathematical derivations. Let us assume that the number of N- and L-cell vortices is $\beta$ and $\alpha$ in one N-cell cycle. The phase shift ($\Delta\Phi_f$) between the N–L vortex pairs with the same serial number (e.g., $k$) in two randomly given neighboring N-cell cycles can be

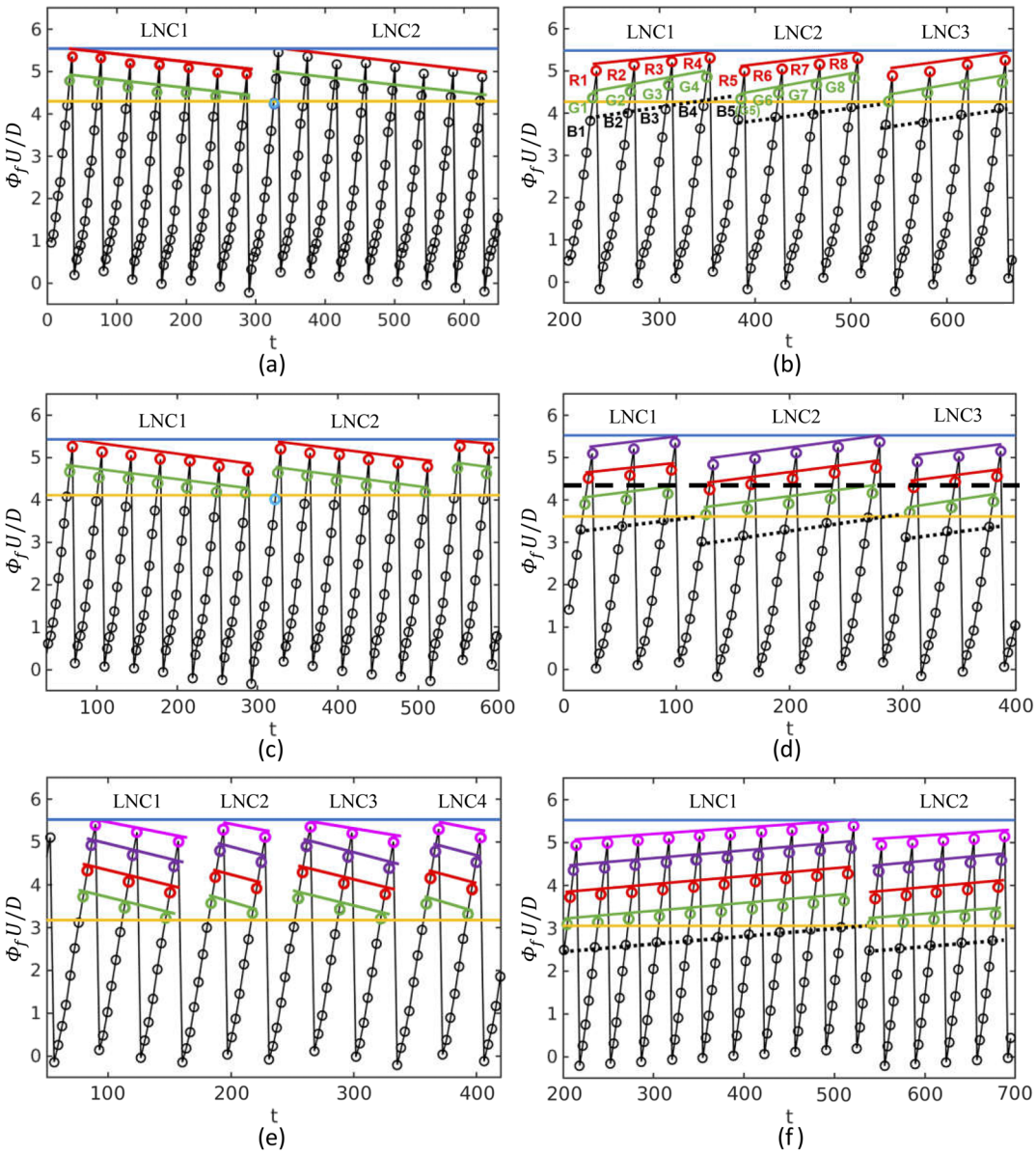


**FIG. 8**. Time trace of $\Phi_f$ between the corresponding N-cell and L-cell vortices in several long N-cell cycles. Results at (a) $D/d$ = 2.0, (b) $D/d$ = 2.2, (c) $D/d$ = 2.4, (d) $D/d$ = 2.6, (e) $D/d$ = 2.8, and (f) $D/d$ = 3.0. In (a), the time $t$ is set to t = t* − 2378.1D/U, where t* is the actual time in the simulation. In (b)–(f), t = t* − 300D/U. The long N-cell cycles are marked by "LNC" with a serial number. The circles represent the $\Phi_f$ between a N-cell vortex and its counterpart L-cell vortex. The green, red, purple, and pink circles indicate the $\Phi_f$, which eventually causes the formation of NL-loop 1, NL-loop 2, NL-loop 3, and NL-loop 4, respectively. Detailed discussions about different NL-loops are given in Sec. IV C. In (b), the red and green circles in the LNC1 and LNC2 are marked by "R" and "G" with its serial number. (All the detailed data about the $\Phi_f$ are included in the supplementary material.) By considering all the highest red points and all the lowest green points, the trigger value and the threshold value are marked by the blue and yellow horizontal lines, respectively. The same method is also used in Fig. 13 of Ref. 17.

measured,

$$\Delta\Phi_f = \Phi_{f_{(i+1,k)}} - \Phi_{f_{(i,k)}}, \tag{6}$$

where $\Phi_{f_{(i+1,k)}}$ and $\Phi_{f_{(i,k)}}$ represent the phase difference of the $k$th N–L vortex pair in the $(i+1)$th and $i$th N-cell cycles, respectively. According to Eq. (4), we can obtain

$$\Phi_{f_{(i,k)}} = \varphi_{N_{k+(i-1)\beta}} - \varphi_{L_{k+(i-1)\alpha}} \tag{7}$$

and reformulate Eq. (6) as

$$\begin{aligned}\Delta\Phi_f &= (\varphi_{N_{k+i\beta}} - \varphi_{L_{k+i\alpha}}) - (\varphi_{N_{k+(i-1)\beta}} - \varphi_{L_{k+(i-1)\alpha}}) \\ &= (\varphi_{N_{k+i\beta}} - \varphi_{N_{k+(i-1)\beta}}) - (\varphi_{L_{k+i\alpha}} - \varphi_{L_{k+(i-1)\alpha}}).\end{aligned} \tag{8}$$

Because the N- and L-cell vortices are spanwise vortices with dominating shedding frequencies, we can obtain

$$\varphi_{N_{k+i\beta}} - \varphi_{N_{k+(i-1)\beta}} = \beta\frac{1}{2f_N}, \tag{9}$$

$$\varphi_{L_{k+i\alpha}} - \varphi_{L_{k+(i-1)\alpha}} = \alpha\frac{1}{2f_L}. \tag{10}$$

Based on Eqs. (5) and (8)–(10), the phase shift between the $k$th N–L vortex pair in neighboring N-cell cycles can be measured as

$$\Delta\Phi_f = \beta\frac{1}{2f_N} - \alpha\frac{1}{2f_L} = -S. \tag{11}$$

One can easily see that positive $S$ causes a decreasing $\Phi_f$ tendency and negative $S$ causes an increasing $\Phi_f$ tendency. This is the first time such a relationship is revealed.

By using the same method as described in Sec. 4 of Ref. 17, Fig. 9 illustrates the relations between $\Phi_f$ and formation positions of the corresponding NL-loop 1 structures during a long N-cell cycle in all six cases. No matter the tendency of $\Phi_f$ is increasing or decreasing, in a specific $D/d$ case, the smaller the $\Phi_f$ is, the more downstream the formation position of NL-loop 1 moves. This observation further supplements and validates the relation between $\Phi_f$ and the formation position of NL-loop 1,[17] as mentioned in Sec. I.

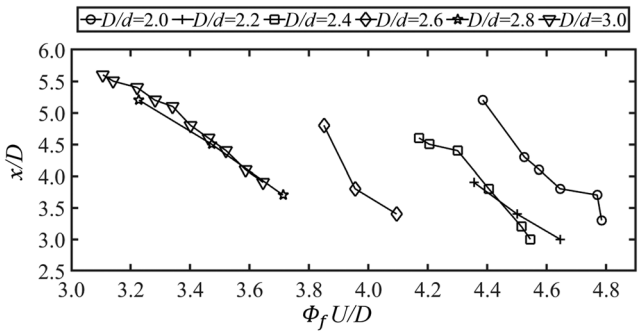


**FIG. 9**. Relation between $\Phi_f$ and the formation position ($x/D$) of the corresponding NL-loop 1 structures in a long N-cell cycle. Details of the formation position of NL-loop 1 in the $D/d$ = 2.2 and 2.4 cases are shown in Figs. 13 and 14, respectively. Other cases are shown in Figs. 22-25 in Appendix B. Information on $\Phi_f$ is included in the supplementary material.

## B. D/d influences on the trigger and threshold values of vortex dislocations

The trigger value and the threshold value, as first defined by Tian *et al.*,[17] are important quantities in a vortex dislocation process. They determine when a vortex dislocation eventually takes place. When $\Phi$ is larger than the trigger value, i.e., the corresponding $\Phi_f$ is larger than the threshold value, vortex dislocations will appear. In the present paper, based on the investigations of the six $D/d$ cases, additional features of the trigger value and the threshold value are discovered.

In Figs. 8(a)–8(f), the trigger value and the threshold value are obtained and shown by the horizontal blue and yellow lines, respectively. Their specific values are listed in Table IV. One can see that although $D/d$ varies, all the six cases approximately share the same trigger value $5.5D/U$. This observation is consistent with McClure *et al.*[13] in which the authors found that the vortex dislocation happens as vortex filaments approach $2\pi$ phase misalignment. The authors assumed that when two neighboring vortex cells simultaneously shed from the shear layer, they have zero phase difference. However, when the slower shedding vortex sheds one shedding period behind the faster shedding vortex cell, the phase difference between them is $2\pi$. In the present paper, a $2\pi$ phase difference is equal to $1/(St_L) \approx 5.5$. In our opinion, this is because the corresponding N- and L-cell vortices are adjacent spanwise vortices on the same side of the step cylinder. When $\Phi_f$ of a N–L vortex pair exceeds one shedding period of the L-cell vortex, the shear layer of the next L-cell vortex on the other side of the step cylinder will cut down this L-cell vortex and induce a vortex dislocation. Furthermore, the number of the N-cell vortices ($\beta$) in one N-cell cycle can be measured as

$$\beta = nint\left(2\frac{1}{St_L}\Big/\left(\frac{1}{St_N} - \frac{1}{St_L}\right)\right) = nint\left(\frac{2St_N}{(St_L - St_N)}\right), \tag{12}$$

where $1/St_L$ is the trigger value (the upper limit of $\Phi_f$), $1/St_N - 1/St_L$ is the accumulating speed of the $\Phi_f$, and *nint* means rounding to the closest integer. Essentially, the only difference between Eqs. (12) and Eq. (1) from Williamson's work[4] is the factor of "2," which is included here to emphasize the importance of counting vortices from the $-Y$ and $+Y$ side independently. Otherwise, it is easy to overlook the antisymmetric vortex interactions. For the same reason, instead of Eq. (2), we propose that the number of the L-cell ($\alpha$) vortex can be measured as

$$\alpha = \beta + 2. \tag{13}$$

Detailed information will be discussed in Sec. IV D.

Different from the constant trigger value, the threshold value continues to decrease as $D/d$ increases from 2.0 to 3.0. Equation (3) shows that for a fixed trigger value, the smaller $\Phi_f$ is, the higher $\Phi_c$ is needed. To reach the same trigger value, the decreasing tendency of the threshold value should be caused by the increasing capacity of $\Phi_c$. In other words, as $D/d$ increases, if the maximum amount of $\Phi_c$ also increases, the vortex dislocation can be triggered with a smaller $\Phi_f$. Further investigations prove this assumption. Due to the spatial inhomogeneity of the convective velocity and the complex vortex interactions, accurate evaluation of $\Phi_c$ is difficult. However, by comparing the distributions of the time-averaged streamwise velocity in different vortex cells regions, the capacity of $\Phi_c$ in different cases can

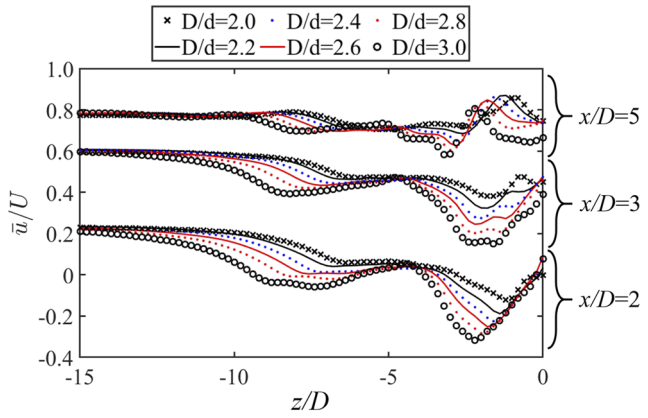


**FIG. 10**. Distributions of the time-averaged streamwise velocity ($\overline{u}/U$) along three vertical sampling lines parallel to the *z*-axis in the center plane ($y/D = 0$) at three positions $x/D = 2$, 3, and 5 in the six $D/d$ cases.

be compared. In Fig. 10, the distributions of time-averaged streamwise velocity ($\overline{u}/U$) in all six cases are plotted. First, in agreement with the conclusion of Tian *et al.*,[17] in the near wake ($x/D = 2$), clear differences between $\overline{u}$ in the N-cell region ($-5 < z/D < 0$) and $\overline{u}$ in the L-cell region ($z/D < -10$) can be observed for all six cases. These differences are substantially reduced when the sampling line moves downstream from $x/D = 2$ to 5. Furthermore, the larger the $D/d$ is, the larger difference in $\overline{u}$ between the N- and L-cell regions can be seen. For example, at $x/D = 2$, the maximum difference between $\overline{u}$ in the N- and L-cell regions is $0.33U$ in the $D/d = 2.0$ case, but reaches $0.54U$ in the $D/d = 3$ case. This observation clearly indicates that comparing to the smaller $D/d$ case, a larger amount of $\Phi_c$ can be accumulated in the larger $D/d$ case.

### C. The number of NL-loop structures

According to Tian *et al.*,[15,17] two NL-loop structures, i.e., NL-loop 1 and NL-loop 2, one NN-loop and one LL-loop were captured in one N-cell cycle in the $D/d = 2.0$ and 2.4 cases. In the present paper, more features of the number of NL-loop structures are investigated.

In Figs. 11(a)–11(e), detailed visualizations of vortex connections and dislocations in the 1st N-cell cycle in the $D/d = 2.6$ case are shown. A corresponding topology sketch is plotted in Fig. 11(f). The short and long vertical straight lines in this figure represent the N- and L-cell vortices, respectively. Between them, the curved solid lines connect the N-cell vortex and its counterpart L-cell vortex. The dashed curves indicate broken connections that were not able to persist due to vortex dislocations. The three NL-loops, i.e., NL-loop 1 N4–L′5, NL-loop 2 N′5–L6, and NL-loop 3 N6–L′7, are marked in green, red, and purple, respectively, in Figs. 11(b)–11(d).

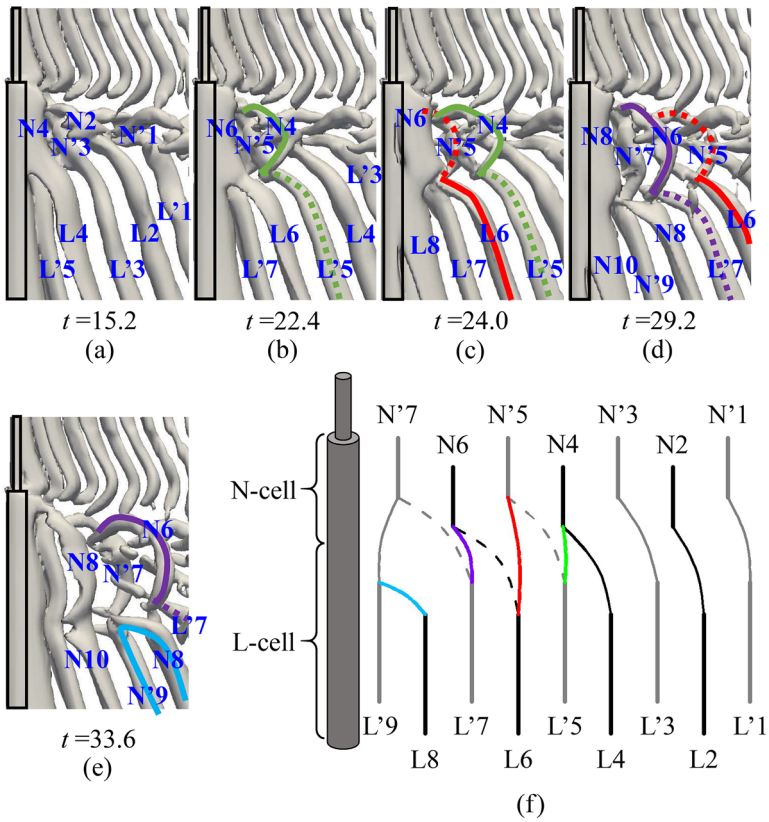


**FIG. 11**. (a)–(e) Isosurface of $\lambda_2 = -0.05$ showing developments of vortex structures on the $-Y$ side in the $D/d = 2.6$ case. Solid and dashed curves indicate the loop structures on the $-Y$ and $+Y$ sides, respectively. (f) Schematic topology illustrating the first N-cell cycle in the $D/d = 2.6$ case. The time $t$ is $t = t^* - 300D/U$, where $t^*$ is the actual time in the simulation.

Compared to the $D/d$ = 2.0 case,[17] as shown in Fig. 6 of Ref. 17, a new NL-loop structure [the purple curve in Fig. 11(d)] forms after NL-loop 2 (the red curve) in the $D/d$ = 2.6 case in Fig. 11. Based on the order of occurrences, the new NL-loop is identified as NL-loop 3, which is believed to be caused by the decreasing threshold value. If we hypothesize that the threshold value in the $D/d$ = 2.6 case was the same as that in the $D/d$ = 2.0 case, the yellow line will move to the black dashed line in Fig. 8(d). This will cause all green circles to become lower than the threshold value. In other words, based on this hypothetical condition, the number of NL-loops will return to 2 in the $D/d$ = 2.6 case, i.e., there will be no vortex dislocation between N′5 and L′5

When $D/d$ continues to increase from 2.6 to 3.0, the threshold value decreases from 3.9 to 3.6. Meanwhile, four NL-loops appear in one N-cell cycle in the $D/d$ = 2.8 and 3.0 cases, as illustrated in Fig. 12. In general, due to the decreasing trend in the threshold value, the number of NL-loops in one N-cell cycle is expected to continuously increase in the higher $D/d$ cases. For a fixed $Re_D$, the maximum number of NL-loops should appear in the free end cylinder case, i.e., when $D/d$ becomes infinite.

### D. Symmetric and antisymmetric vortex interactions

Antisymmetric vortex interactions were reported and discussed in the wake behind the single step cylinders with $D/d$ = 2.0 and 2.4 by Tian *et al.*[15,17] In the present manuscript, by investigating four extra cases $D/d$ = 2.2, 2.6, 2.8, and 3, an additional symmetric vortex interaction is observed. As examples, the NL-loop 1 structures in the neighboring N-cell cycles are plotted in the D/d = 2.2 and 2.4 cases in Figs. 13 and 14, respectively. The NL-loop 1 structures continuously appear at the −Y side of the step cylinder in Figs. 13(a)–13(d). We call this symmetric vortex interaction in contrast to the antisymmetric vortex interaction shown in Fig. 14. From the information in Table IV, we learn that in a certain $D/d$ case, whether vortex dislocations are symmetric or antisymmetric is determined by the parity of the number of N- and L-cell vortices, i.e., $\beta$ and $\alpha$, in one N-cell cycle. When $\beta$ and $\alpha$ are even numbers, symmetric vortex interactions will appear. Oppositely, when $\beta$ and $\alpha$ are odd numbers, antisymmetric vortex interactions will happen. This is because both the N- and L-cell vortices are shed alternatingly from the +Y and −Y side of the step cylinder. When there are an even number of N- and L-cell vortices between the corresponding NL-loop 1 structures in the neighboring N-cell cycles, these NL-loop 1 structures appear at the same side of the step cylinder, i.e., symmetric vortex interactions. Otherwise, conventional antisymmetric vortex interactions appear.

Long time observations reveal that not only the decreasing tendency of $\Phi_f$ but also the increasing tendency of $\Phi_f$ can occasionally interrupt the continuous symmetric and antisymmetric vortex interactions. As described in Sec. I, when the corresponding $\Phi_f$ continues to decrease in subsequent N-cell cycles, one additional N–L vortex pair will be needed in a certain N-cell cycle to make $\Phi_f$ sufficiently large to induce the formation of the NL-loop structure. It is this

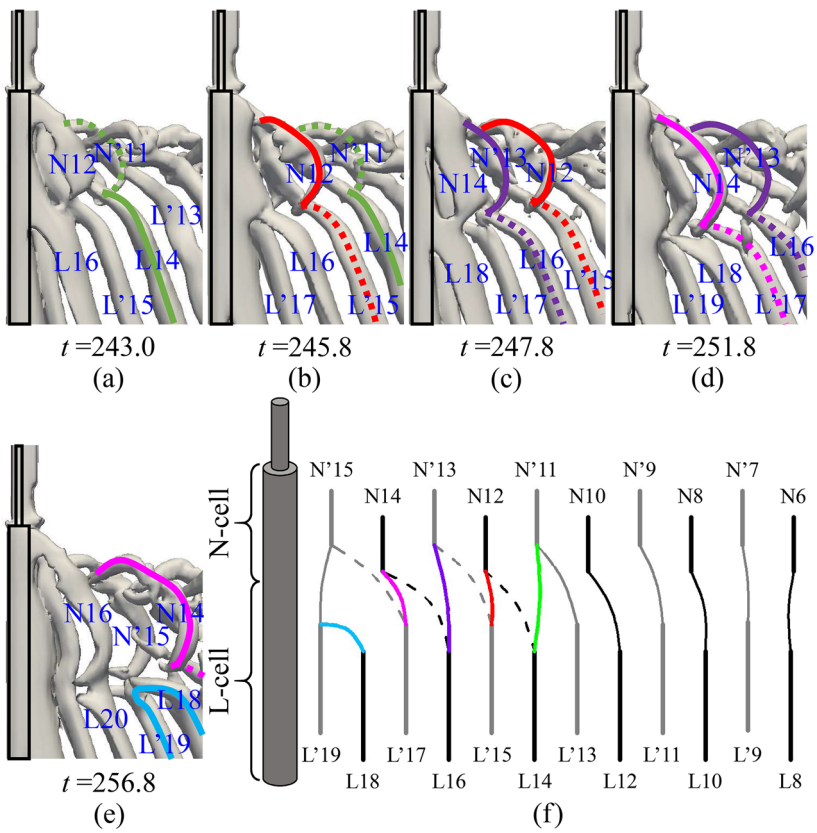


**FIG. 12.** (a)–(e) Isosurface of $\lambda_2 = -0.05$ showing developments of vortex structures on the $-Y$ side in the $D/d$ = 3.0 case. Solid and dashed curves indicate the loop structures on the $-Y$ and $+Y$ sides, respectively. (f) Schematic topology illustrating the first N-cell cycle in the $D/d$ = 3.0 case. The time $t$ is t = t* − 300D/U, where t* is the actual time in the simulation.

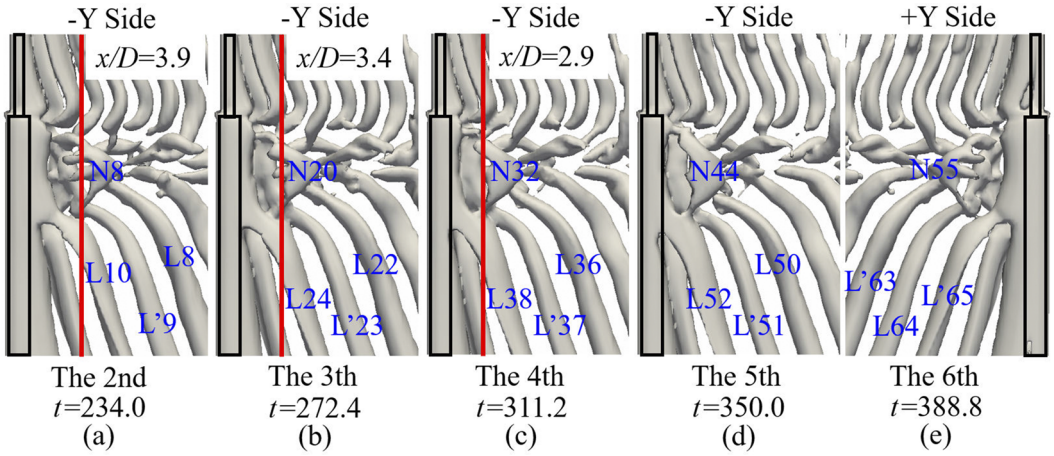


**FIG. 13**. [(a)–(e)] The just-formed NL-loop 1 structures in the first to sixth N-cell cycles are plotted from both the −Y and +Y side in the $D/d$ = 2.2 case. The red line marks the formation position of NL-loop 1. The time $t$ is set to $t = t^* - 300D/U$.

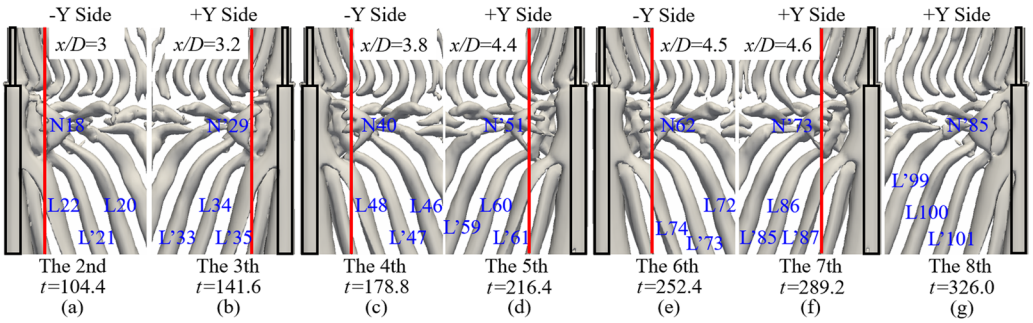


**FIG. 14**. [(a)–(g)] The just-formed NL-loop 1 structures in the second to eighth N-cell cycles are plotted from both the −Y and +Y sides in the $D/d$ = 2.4 case. The red line marks the formation position of NL-loop 1. The time $t$ is set to $t = t^* - 300D/U$.

one additional N–L vortex pair that changes the parity of the number of N- and L-cell vortices and further causes the interruption of the repetitive symmetric or antisymmetric vortex interactions. For the present cases with the discovered increasing tendency of $\Phi_f$, the interruption works in a different way.

In Figs. 8(b), 8(d), and 8(f), the black dotted lines illustrate the increasing tendency of $\Phi_f$ of the N–L vortex pair, which is just before the N–L vortex pair whose dislocation finally causes the formation of NL-loop 1. In the $D/d$ = 2 case, along the black dotted line in Fig. 8, $\Phi_f$ increases from B1 to B5 and eventually exceeds the threshold value in the fifth N-cell cycle (B5). Under this circumstance, by including the contribution of $\Phi_c$, $\Phi$ is large enough to induce the formation of NL-loop 1 (N′55–L64) in Fig. 13(e). Between neighboring NL-loop 1 structures in Figs. 13(a)–13(d), there are 12 N- and 14 L-cell vortices. However, between Figs. 13(d) and 13(e), there are only 11 N- and 13 L-cell vortices in the fifth N-cell cycle, i.e., one N–L vortex pair less than in previous N-cell cycles. It is this one less N–L vortex pair that causes the NL-loop 1 structure (N′55–L64) to form at the +Y side of the step cylinder and interrupts the continuous symmetric vortex interactions. Similar situations are also observed in the $D/d$ = 2.6 and 3.0 cases, which are included in Figs. 26–29 in Appendix C. In general, when $\Phi_f$ in advance becomes smaller or larger than the threshold value, one more or one less N–L vortex pair will change the parity of the number of N- or L-cell vortices in one N-cell cycle and further interrupt the continuously symmetric or antisymmetric vortex interactions. This new relationship could help to understand the vortex dynamics in a vortex dislocation process more clearly.

## V. LIKELIHOOD ANALYSIS

It is striking to see from Table IV that among the six cases we investigated here, three cases have the increasing tendency of $\Phi_f$, and the other three have the decreasing tendency. Moreover, three cases show symmetric vortex interactions, while the other three show antisymmetric vortex interactions. It is hard to believe that these equal occurrences are all by coincidence. Therefore, we present a likelihood analysis here. Based on $St_N$ and $St_L$, we can obtain

$$E_N = 2St_N/(St_L - St_N), \tag{14}$$

$$E_L = 2St_L/(St_L - St_N), \tag{15}$$

where $E_N$ and $E_L$ are the exact values compared to the rounding value $\alpha$ in Eq. (12). The differences ($\delta$, $\delta_N$, and $\delta_L$) between the exact values ($E_N$ and $E_L$) and the rounding values ($\beta$ and $\alpha$) can be expressed as follows:

$$\delta_N = E_N - \beta, \tag{16}$$

$$\delta_L = E_L - \alpha. \tag{17}$$

According to Eqs. (12) and (13), one can easily obtain

$$\delta = \delta_N = \delta_L. \tag{18}$$

Based on Eqs. (16)–(18), the original equation (5) can be rewritten as

$$\frac{SU}{D} = \alpha\frac{1}{2St_L} - \beta\frac{1}{2St_N} = (E_L - \delta_L)\frac{1}{2St_L} - (E_N - \delta_N)\frac{1}{2St_N} = \delta\left(\frac{1}{2St_N} - \frac{1}{2St_L}\right). \tag{19}$$

Due to the fact that the N-cell vortices shed slower than the L-cell vortices, i.e., $St_N$ is always smaller than $St_L$, and the value of both $U$ and $D$ are positive, the sign of the $S$ value in Eq. (19) is determined by the sign of $\delta$. In other words, when $E_N$ and $E_L$ are rounded to smaller $\beta$ and $\alpha$, respectively, e.g., in the $D/d$ = 2.0, 2.4, and 2.8 cases, the corresponding $\delta$ value and the $S$ value become positive. Consequently, a decreasing tendency of $\Phi_f$ appears, e.g., as shown in Figs. 8(a), 8(c), and 8(e). Otherwise, negative $\delta$ and $S$ lead to an increasing tendency of $\Phi_f$. Meanwhile, based on the parity of $\beta$ and $\alpha$, the characteristic of vortex interactions (symmetry or antisymmetry) can be deduced. Relations between $E_N$ and features of vortex dislocations are shown in Table V.

In Fig. 15(a), $E_N$ in the six cases are shown as six black circles. By applying a fifth order interpolation polynomial in curve fitting to these six circles, the black curve in Fig. 15(a) is obtained to describe the relation between $E_N$ and $D/d$. The justification of this curve is checked by simulating four more cases, i.e., the $D/d$ = 2.1, 2.3, 2.5, and 2.7 cases. After following the same simulation and analysis processes as described in Sec. IV, information on these four cases is shown in Table VI. More detailed information is included in Figs. 26–29 in Appendix C. By using Eq. (14), four red circles are plotted in Fig. 15(a), which fit the black curve very well. This indicates a reasonable curve fitting. Based on this curve and Table V, Fig. 15(b) can be sketched to show the different characteristics for all cases between $D/d$ = 2 and 3. One can easily see that the total area of the red bar is larger than that of the green bar. On the other hand, the total areas of the black and white bars

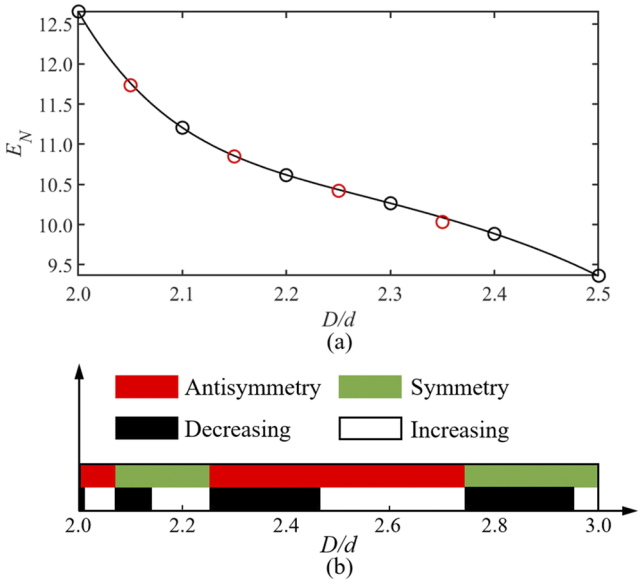


**FIG. 15**. (a) $E_N$ in the $D/d$ = 2.0, 2.2, 2.4, 2.6, 2.8, and 3.0 cases are marked by black circles. By applying a fifth order interpolation polynomial in curve fitting on these six circles, the black curve [$E_N = -5.706(D/d)^5 + 77.805(D/d)^4 - 426.295(D/d)^3 + 1171.735(D/d)^2 - 1615.737(D/d) + 905.749$] is obtained to describe the relation between $E_N$ and $D/d$. Moreover, $E_N$ in the $D/d$ = 2.1, 2.3, 2.5, and 2.7 cases are plotted as red circles to justify the curve fitting function. (b) Following the relation between $E_N$ and characteristics of vortex dislocations in Table V, the black, white, red, and green bars are plotted to show the cases with decreasing $\Phi_f$ tendency, the cases with increasing $\Phi_f$ tendency, the cases with antisymmetric vortex interactions, and the cases with symmetric vortex interactions, respectively.

are almost the same. Therefore, we can anticipate that when $D/d$ is randomly chosen between 2 and 3, the likelihood of increasing $\Phi_f$ and decreasing $\Phi_f$ tendencies is almost the same, whereas the likelihood of antisymmetric vortex interactions is larger than that of symmetric vortex interactions. This anticipation agrees well with our observations shown in Table VI. In these four additional cases, the increasing $\Phi_f$ tendency appears in two cases, i.e., the $D/d$ = 2.5 and 2.7 cases. The other two cases show decreasing $\Phi_f$ tendency. However, only the $D/d$ = 2.1 case shows the symmetric vortex interactions. Antisymmetric vortex interactions are observed in the other three cases. The present result indicates that the characteristics of the vortex dislocations are determined by the shedding frequencies

**TABLE V**. Relation between $E_N$ and characteristics of vortex dislocations. In the first column, $n$ represents natural numbers ($n$ = 1, 2, 3, . . .).

| $E_N$ | Tendency of $\Phi_f$ | Symmetry or antisymmetry |
|---|---|---|
| $2n - 1 < E_N < 2n - 0.5$ | Decrease | Antisymmetry |
| $2n - 0.5 < E_N < 2n$ | Increase | Symmetry |
| $2n < E_N < 2n + 0.5$ | Decrease | Symmetry |
| $2n + 0.5 < E_N < 2n + 1$ | Increase | Antisymmetry |

**TABLE VI**. Detailed information on vortex dislocations in other four $D/d$ cases, i.e., $D/d$ = 2.1, 2.3, 2.5, and 2.7.

| $D/d$ | $St_N$ | $St_L$ | $\beta$ | $\alpha$ | Symmetry or antisymmetry | SU/D | Tendency of $\Phi_f$ |
|---|---|---|---|---|---|---|---|
| 2.1 | 0.1529 | 0.1779 | 12 | 14 | Symmetry | 0.107 | Decrease |
| 2.3 | 0.1509 | 0.1775 | 11 | 13 | Antisymmetry | 0.172 | Decrease |
| 2.5 | 0.1496 | 0.1777 | 11 | 13 | Antisymmetry | −0.042 | Increase |
| 2.7 | 0.1485 | 0.1767 | 11 | 13 | Antisymmetry | −0.252 | Increase |

of the N- and L-cell vortices. Meanwhile, as described in Sec. III B, by affecting the 3D effects (downwash and increased base pressure), the changed diameter ratio influences the shedding frequencies of the N- and L-cell vortices and the corresponding $E_N$, which, in turn, affects the characteristics of vortex dislocations. The likelihood of antisymmetric or symmetric vortex interactions and increasing or decreasing $\Phi_f$ tendencies is determined by the relation between $E_N$ and $D/d$.

## VI. CONCLUSION

In the present paper, we use DNS to investigate vortex dynamics in the near wake behind single step cylinders with $2 \le D/d \le 3$ at $Re_D = 150$. Our results are consistent with previous studies,[1,11,15,17] with respect to the mainly three dominating spanwise vortices (i.e., S-, N-, and L-cell vortices) and some interesting characteristics of vortex dislocations [i.e., two phase-difference accumulation mechanisms ($\Phi = \Phi_f + \Phi_c$), the NL-loop structures appearing in the dislocation process, the trigger and threshold values of vortex dislocations, antisymmetric vortex interactions between neighboring N-cell cycles, and its interruptions]. In addition, the numerical results provide deeper and more complete information on step cylinder wakes.

First, by a fast Fourier transform (FFT) of time series of the streamwise velocity $u$, shedding frequencies and extensions of three spanwise vortex cells are investigated. As $D/d$ increases from 2 to 3, the extension of the S-cell vortex remains almost constant. The shedding frequency of the S-cell vortex ($St_S$) is simply dependent on $Re_d$. Meanwhile, an expansion of the N-cell region and a shrinking of the L-cell region are observed. For the first time, we report that as $D/d$ increases, the N–L transition region continues to move toward the large cylinder part, and its length gradually increases. Since the N-cell region being closer to the step position than the L-cell region, when $D/d$ increases, the shedding frequency of the N-cell vortex ($St_N$) decreases faster than the shedding frequency of the L-cell vortex ($St_L$). The oblique shedding angle ($\theta_L$) of the L-cell vortex remains almost unaffected. In the large cylinder part, the strength of the induced downwash flow ($-w/U$) and the base pressure become larger, when $D/d$ increases. By carefully checking the distributions of $-w/U$ and base pressure coefficient ($C_{pb}$), we conclude that the formation of N-cell vortices is caused by the joint influence of both increased $-w/U$ and increased $C_{pb}$, but the latter one plays a major role.

Moreover, based on long-time observations on iso-surfaces of $\lambda_2$, we found that in the $D/d = 2.2$, 2.8, and 3.0 cases, the NL-loop 1 structure continues to appear at either the +Y or −Y side of the step cylinder. In comparison with the already known antisymmetric phenomenon,[15,17] we call this symmetric vortex interactions. By analyzing the number of N- and L-cell vortices, i.e., $\beta$ and $\alpha$, in one N-cell cycle in different $D/d$ cases, we found that it is the parity of $\beta$ and $\alpha$ that determines whether symmetric or antisymmetric vortex interactions appears in a certain $D/d$ case.

By using a reliable phase tracking method, we monitored the time trace of $\Phi_f$ in the $D/d = 2.0$, 2.2, 2.4, 2.6, 2.8, and 3.0 cases. An increasing tendency of $\Phi_f$ is first captured in $D/d = 2.2$, 2.6, and 3.0 cases. In these cases, the formation position of NL-loop 1 structures is observed to continuously move upstream as $\Phi_f$ increases. Similar to the decreasing tendency of $\Phi_f$ reported in Ref. 17, the discovered increasing $\Phi_f$ tendency can also cause the interruption of continuous antisymmetric or symmetric vortex interaction phenomena, but in a different way. According to the time trace of $\Phi_f$, the trigger value of vortex dislocations is found to remain constant when $D/d$ varies. The threshold value of vortex dislocations decreases as D/d increases, which further causes the number of NL-loop structures in one N-cell cycle to increase from 2 in the $D/d = 2.0$ case to 4 in the $D/d = 3.0$ case. Based on the application of a constant trigger value, we propose Eqs. (12) and (13) to measure $\beta$ and $\alpha$. Comparing with the conventional Eqs. (1) and (2), a new factor of "2" is introduced to emphasize the importance of counting vortices from the −Y and +Y sides independently. Otherwise, the antisymmetric phenomenon is easily overlooked. Furthermore, a universal rule of anticipating the qualitative features of vortex dislocations is summarized in Table V.

Finally, we analyze the likelihood of appearance of antisymmetric or symmetric vortex interactions and the likelihood of increasing or decreasing phase differences. Based on the investigations of $D/d = 2.0$, 2.2, 2.4, 2.6, 2.8, and 3.0 cases, we predicted that when $2 \le D/d \le 3$, the likelihood of increasing $\Phi_f$ and decreasing $\Phi_f$ is almost the same, but the antisymmetric phenomenon is more likely to appear than the symmetric phenomenon. Further observations in $D/d = 2.1$, 2.3, 2.5, and 2.7 cases prove our anticipation.

In summary, by simulating altogether 10 different $D/d$ cases, the present paper provides a more in-depth and complete understanding of the vortex dislocation phenomenon. Some new observations, e.g., an increasing tendency of $\Phi_f$, the symmetric features, and the increased number of NL-loop structures in the vortex dislocation process, help to outline a better picture and lead to the identification of several important relationships. These include the relationship between $\alpha$ ($\beta$) and (anti-)symmetry and the relationship between tendency of $\Phi_f$ and $S$. Moreover, the method and formulas we used to analyze the likelihood of appearance of different features of vortex dislocations may also be applicable in other wake flows.

## SUPPLEMENTARY MATERIAL

By using the phase tracking method described in Ref. 17, the phase information on N- and L-cell vortices and their phase differences in the $D/d = 2.0$, 2.2, 2.4, 2.6, 2.8, and 3.0 cases are shown in the supplementary material. The N–L vortex pair whose phase difference induces vortex dislocations is highlighted in gray.

## ACKNOWLEDGMENTS

Computing resources were granted by the Norwegian Research Council (Program for Supercomputing) under project nn9191k. C.T. would like to thank the China Scholarship Council (CSC) for financial support.

## APPENDIX A: STREAMWISE VELOCITY SPECTRA IN THE $D/d$ = 2.0, 2.2, 2.4, 2.6, 2.8, AND 3.0 CASES

This appendix includes six figures, i.e., Figs. 16–21. All velocity spectra are calculated by a fast Fourier transform (FFT) of at least $2000D/U$ continuous streamwise velocity ($u$) data along a vertical sampling line parallel to the $z$-axis with density $0.2D$ positioned at $(x/D, y/D) = (1.6, 0.4)$.

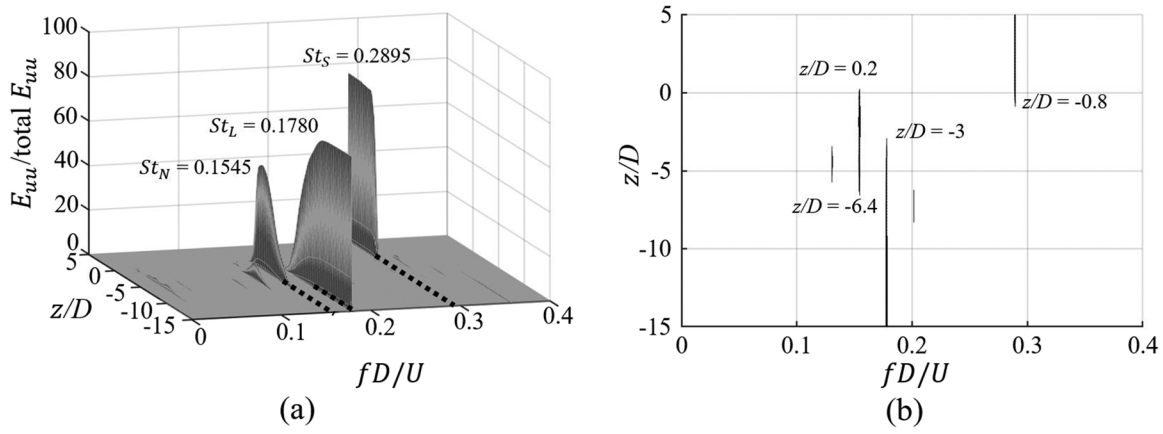


**FIG. 16**. In the $D/d$ = 2.0 case, (a) a 3D version of velocity spectra along a spanwise line behind the step cylinder at ($x/D$, $y/D$) = (1.6, 0.4), where the shedding frequencies of the three main vortex cells (S-cell: $St_S = f_S D/U$, N-cell: $St_N = f_N D/U$, and L-cell: $St_L = f_L D/U$) are marked. (b) Projection of the 3D plot in (a) into the horizontal plane. Only points with $E_{uu}$/(total $E_{uu}$) ≥ 4 are shown.

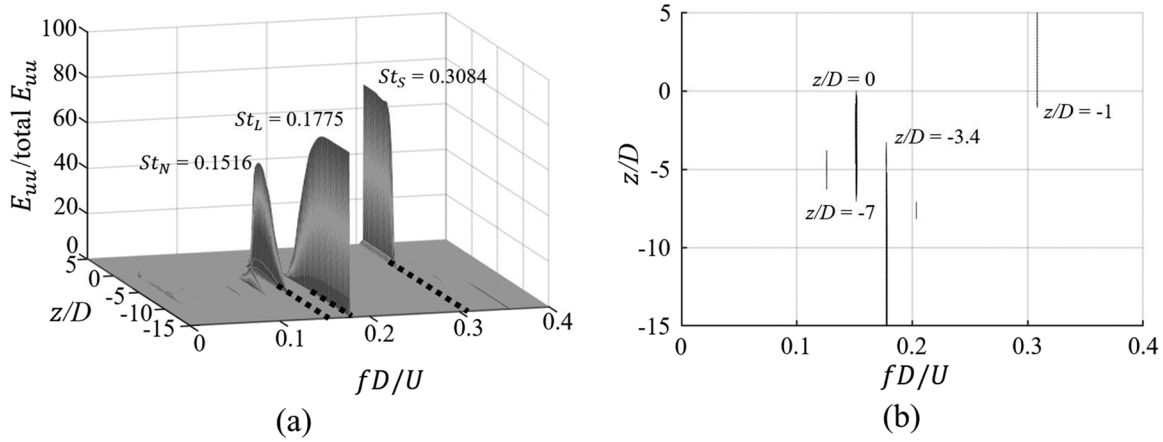


**FIG. 17**. (a) and (b) are the same as Figs. 16(a) and 16(b), but in a different case $D/d$ = 2.2.

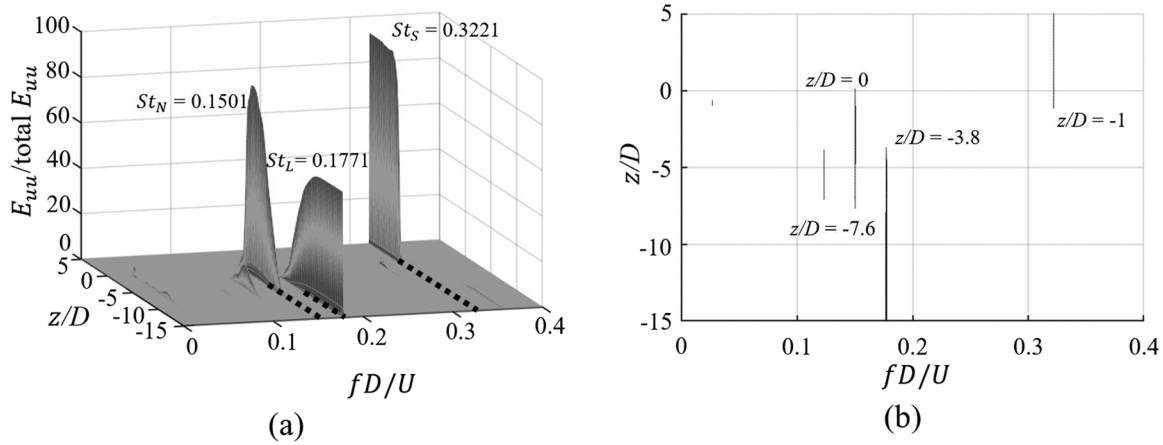


**FIG. 18**. (a) and (b) are the same as Figs. 16(a) and 16(b), but in a different case $D/d$ = 2.4.

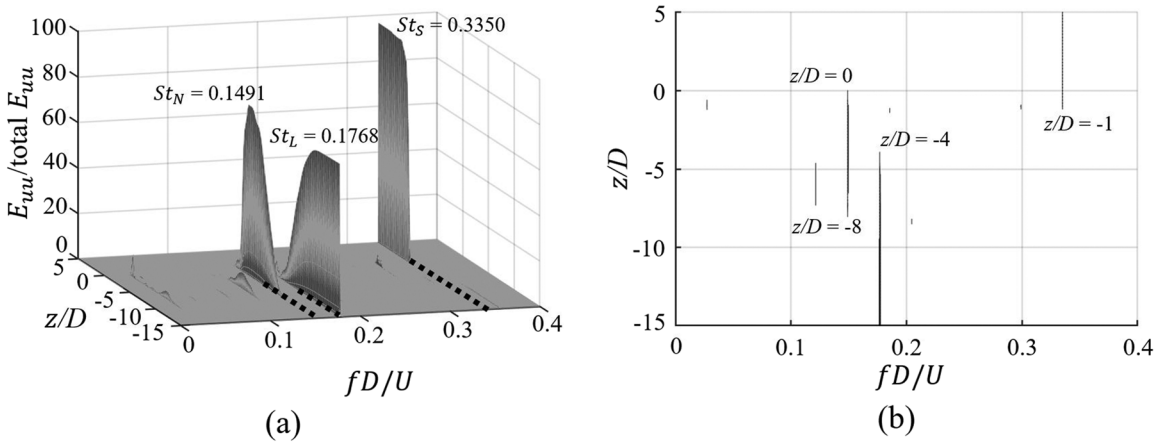


**FIG. 19**. (a) and (b) are the same as Figs. 16(a) and 16(b), but in a different case $D/d = 2.6$.

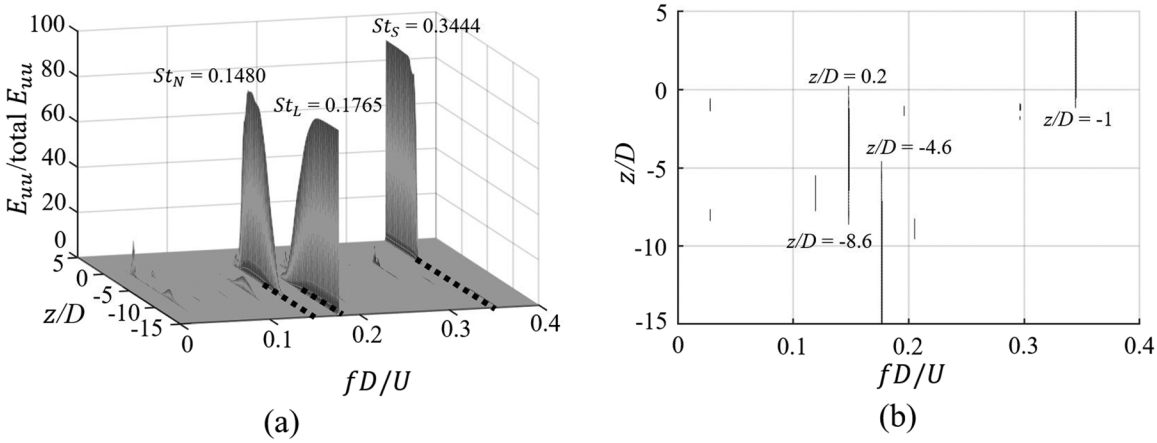


**FIG. 20**. (a) and (b) are the same as Figs. 16(a) and 16(b), but in a different case $D/d = 2.8$.

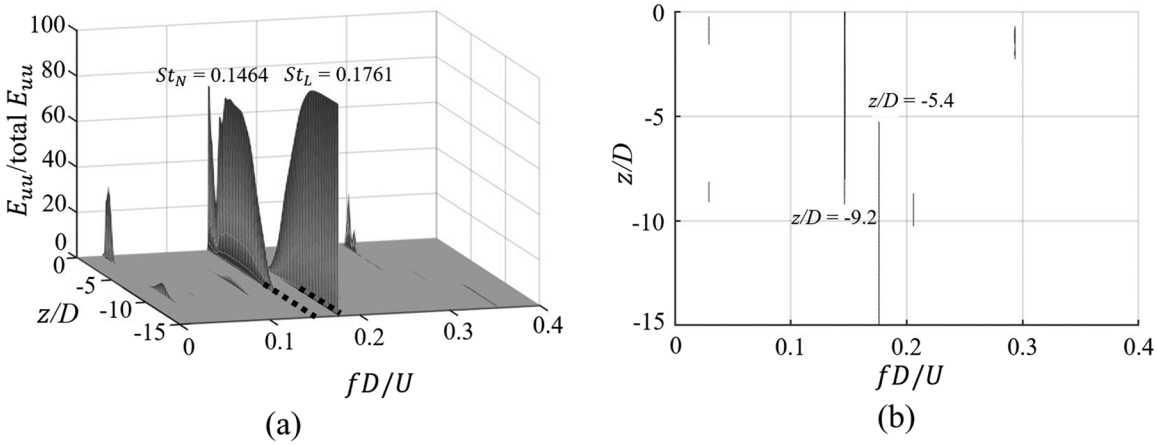


**FIG. 21**. (a) and (b) are the same as Figs. 16(a) and 16(b), but in a different case $D/d = 3.0$.

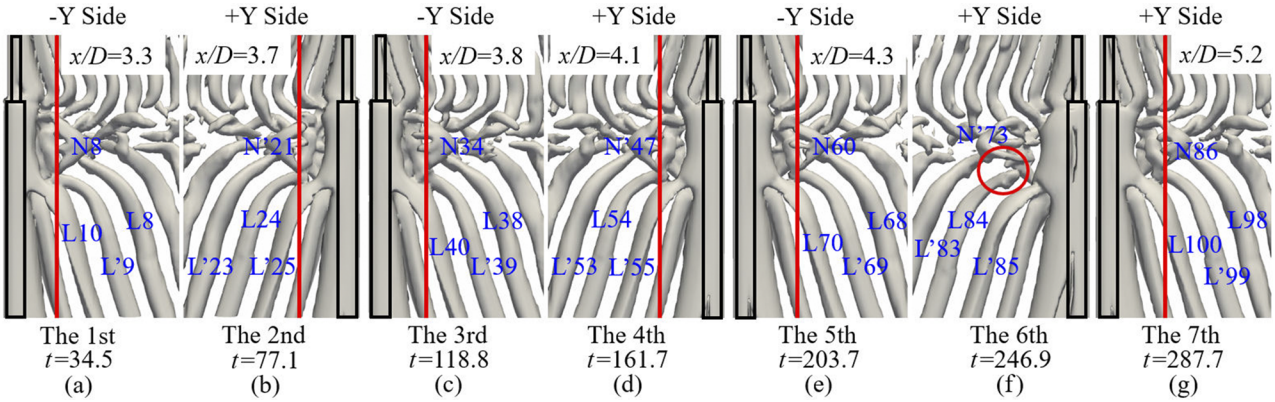


**FIG. 22**. [(a)–(g)] Isosurfaces of $\lambda_2 = -0.05$ showing the formation position and the side of the NL-loop 1 structure in the first long N-cell cycle in the $D/d$ = 2.0 case. The antisymmetric phenomenon appears. The red circle in panel (f) highlights an irregular absence of the NL-loop 1 structure, which was discussed in Ref. 17. The time $t$ is set to $t = t^* - 2378.1D/U$.

## APPENDIX B: DETAILED INFORMATION ON VORTEX DISLOCATIONS IN THE $D/d$ = 2.0, 2.6, 2.8, AND 3.0 CASES

In this appendix, the just-formed NL-loop 1 structures in the first long N-cell cycle are plotted in the $D/d$ = 2.0, 2.6, 2.8, and 3.0 cases from both the $-Y$ and $+Y$ sides (in Figs. 22, 23, 24, and 25, respectively). The red line marks the formation position of NL-loop 1. As discussed in Sec. IV D, when the NL-loop 1 structure appears alternately at the $+Y$ and $-Y$ sides between subsequent N-cell cycles, the antisymmetric vortex interactions appear. On the other hand, when the NL-loop 1 structure continuously appears at the $+Y$ or $-Y$ side in the neighboring N-cell cycles, the symmetric vortex interactions appear.

## APPENDIX C: DETAILED INFORMATION IN $D/d$ = 2.1, 2.3, 2.5, AND 2.7 CASES

This appendix includes four figures, i.e., Figs. 26–29. All velocity spectra are calculated by a fast Fourier transform (FFT) of at least $2000D/U$ continuous streamwise velocity ($u$) data along a vertical sampling line parallel to the $z$-axis with density $0.2D$ positioned at $(x/D, y/D) = (1.6, 0.4)$. The just-formed NL-loop 1 structures in the first long N-cell cycle are plotted in the $D/d$ = 2.1, 2.3, 2.5, and 2.7 cases from both the $-Y$ and $+Y$ sides. The red line marks the formation position of NL-loop 1. As discussed in Sec. IV D, when the NL-loop 1 structure appears alternately at the $+Y$ and $-Y$ sides between subsequent N-cell cycles, the antisymmetric vortex interactions appear. On the other hand, when the NL-loop 1 structure

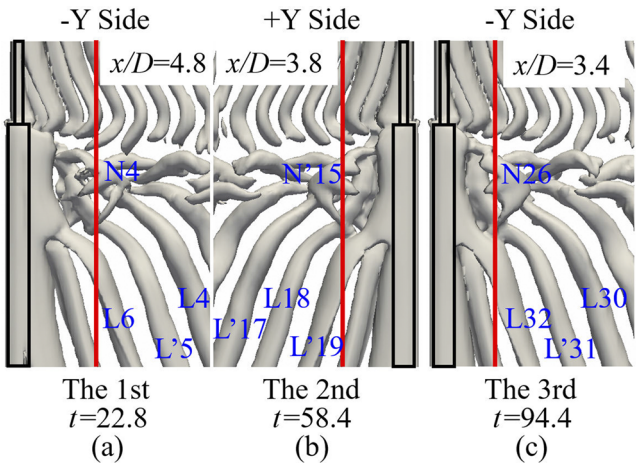


**FIG. 23**. [(a)–(c)] Isosurfaces of $\lambda_2 = -0.05$ showing the formation position and the side of the NL-loop 1 structure in the first long N-cell cycle in the $D/d$ = 2.6 case. The antisymmetric phenomenon appears. The time $t$ is set to $t = t^* - 300D/U$.

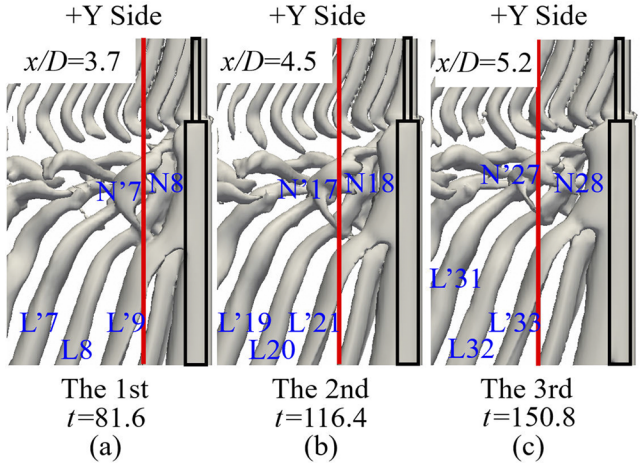


**FIG. 24**. [(a)–(c)] Isosurface of $\lambda_2 = -0.05$ showing the formation position and the side of the NL-loop 1 structure in the first long N-cell cycle in the $D/d$ = 2.8 case. The symmetric phenomenon appears. The time $t$ is set to $t = t^* - 300D/U$.

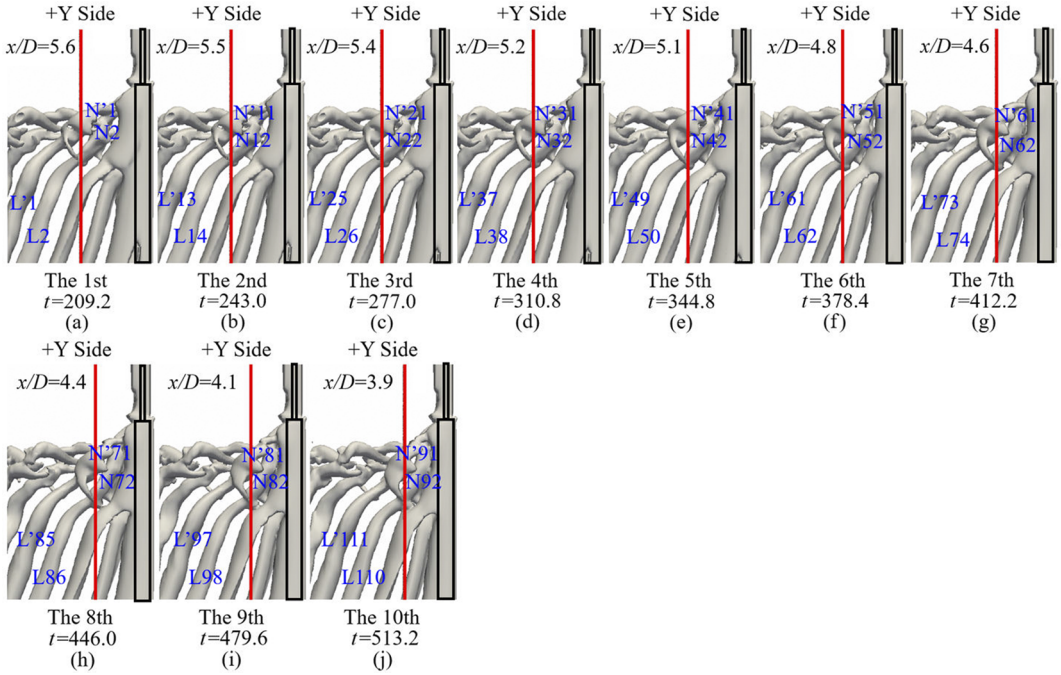


**FIG. 25**. [(a)–(j)] Isosurface of $\lambda_2 = -0.05$ showing the formation position and the side of the NL-loop 1 structure in the first long N-cell cycle in the $D/d = 3.0$ case. The symmetric phenomenon appears. The time $t$ is set to $t = t^* - 300D/U$.

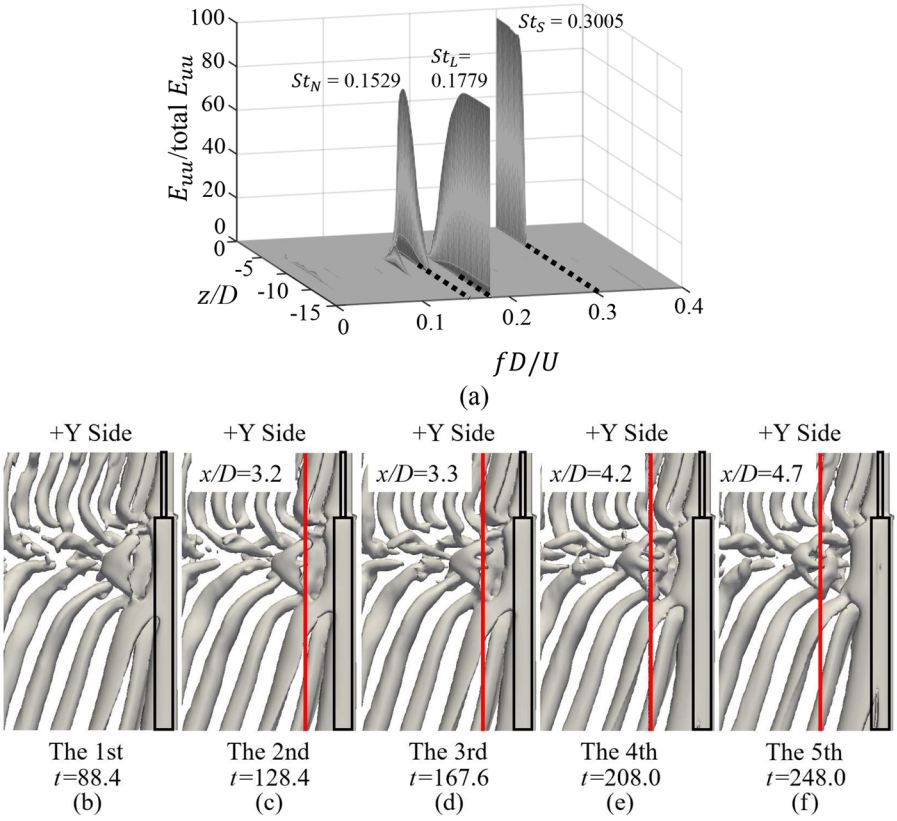


**FIG. 26**. In the $D/d = 2.1$ case: (a) 3D velocity spectra along a spanwise line behind the step cylinder at $(x/D, y/D) = (1.6, 0.4)$, where the shedding frequencies of the three main vortex cells (S-cell: $St_S = f_S D/U$, N-cell: $St_N = f_N D/U$, and L-cell: $St_L = f_L D/U$) are marked. [(b)–(f)] Isosurface of $\lambda_2 = -0.05$ showing the formation position and the side of the NL-loop 1 structure in the first long N-cell cycle in the $D/d = 2.1$ case. The symmetric phenomenon and decreasing tendency of $\Phi_f$ appear. The time $t$ is set to $t = t^* - 300D/U$.

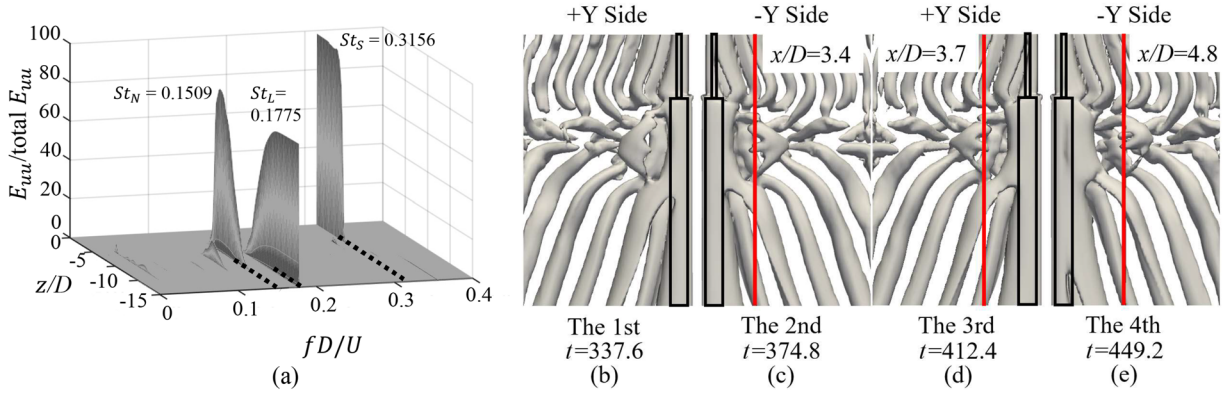


**FIG. 27**. (a) is the same as Fig. 26(a), but in a different case $D/d$ = 2.3. [(b)–(e)] Isosurface of $\lambda_2 = -0.05$ showing the formation position and the side of the NL-loop 1 structure in the first long N-cell cycle in the $D/d$ = 2.3 case. The antisymmetric phenomenon and decreasing tendency of $\Phi_f$ appear. The time $t$ is set to $t = t^* - 300D/U$.

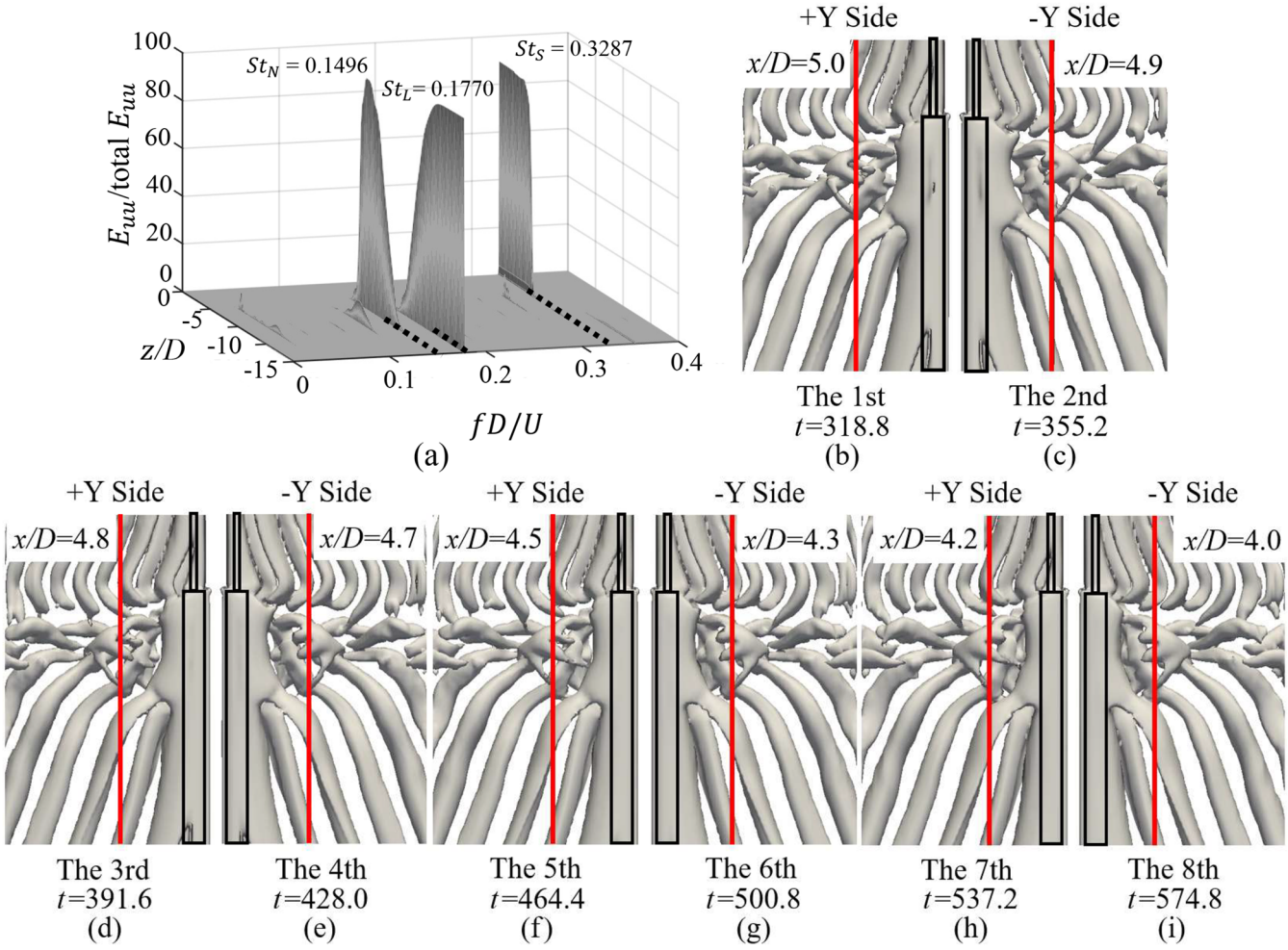


**FIG. 28**. (a) is the same as Fig. 26(a), but in a different case $D/d$ = 2.5. [(b)–(i)] Isosurface of $\lambda_2 = -0.05$ showing the formation position and the side of the NL-loop 1 structure in the first long N-cell cycle in the $D/d$ = 2.5 case. The antisymmetric phenomenon and increasing tendency of $\Phi_f$ appear. The time $t$ is set to $t = t^* - 300D/U$.

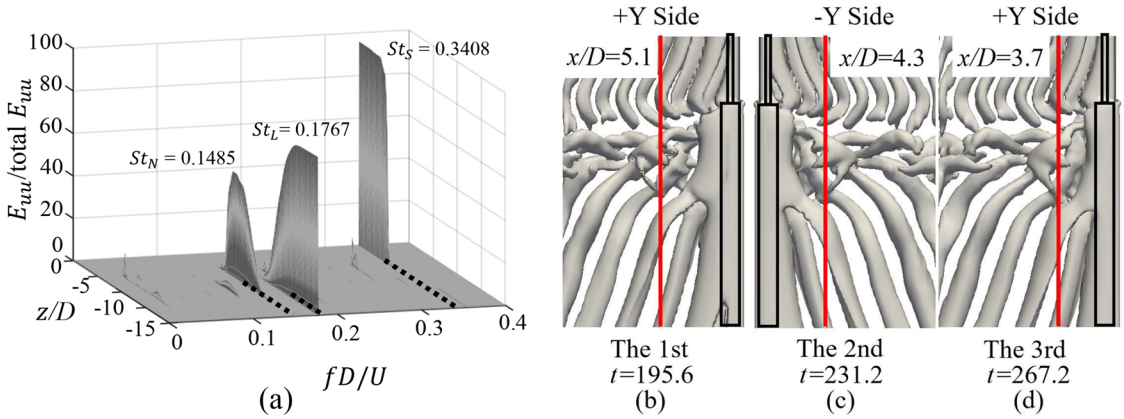


**FIG. 29**. (a) is the same as Fig. 26(a), but in a different case $D/d$ = 2.7. [(b)–(d)] Isosurface of $\lambda_2 = -0.05$ showing the formation position and the side of the NL-loop 1 structure in the first long N-cell cycle in the $D/d$ = 2.7 case. The antisymmetric phenomenon and increasing tendency of $\Phi_f$ appear. The time $t$ is set to $t = t^* - 300D/U$.

continuously appears at the $+Y$ or $-Y$ side in the neighboring N-cell cycles, the symmetric vortex interactions appear. Based on Sec. IV A, by observing the tendency of the formation position of NL-loop 1 structures, the variation in $\Phi_f$ can be obtained. When the formation position of NL-loop 1 structures continuously moves downstream or upstream in a long N-cell cycles, the corresponding decreasing or increasing tendency of $\Phi_f$ appears, respectively.

## DATA AVAILABILITY

The data that support the findings of this study are available from the corresponding author upon reasonable request.

## REFERENCES

[1]W. Dunn and S. Tavoularis, "Experimental studies of vortices shed from cylinders with a step-change in diameter," J. Fluid Mech. **555**, 409–437 (2006).
[2]C. G. Lewis and M. Gharib, "An exploration of the wake three dimensionalities caused by a local discontinuity in cylinder diameter," Phys. Fluids A **4**, 104–117 (1992).
[3]A. Ayoub and K. Karamcheti, "An experiment on the flow past a finite circular cylinder at high subcritical and supercritical Reynolds numbers," J. Fluid Mech. **118**, 1–26 (1982).
[4]C. H. K. Williamson, "Oblique and parallel modes of vortex shedding in the wake of a circular cylinder at low Reynolds numbers," J. Fluid Mech. **206**, 579–627 (1989).
[5]F. Jiang, B. Pettersen, H. I. Andersson, J. Kim, and S. Kim, "Wake behind a concave curved cylinder," Phys. Rev. Fluids **3**, 094804 (2018).
[6]M. M. Zdravkovich, V. P. Brand, G. Mathew, and A. Weston, "Flow past short circular cylinders with two free ends," J. Fluid Mech. **203**, 557–575 (1989).
[7]C. Morton, S. Yarusevych, and I. Carvajal-Mariscal, "Study of flow over a step cylinder," Appl. Mech. Mater. **15**, 9–14 (2009).
[8]P. W. Bearman, "Investigation of the flow behind a two-dimensional model with a blunt trailing edge and fitted with splitter plates," J. Fluid Mech. **21**, 241–255 (1965).
[9]C. Norberg, "An experimental study of the flow around cylinders joined with a step in diameter," in *Proceedings of the 11th Australasian Fluid Mechanics Conference, Hobart, Australia* (University of Tasmania, 1992), Vol. 1, pp. 507–510.
[10]B. Vallès, H. I. Andersson, and C. B. Jenssen, "Direct-mode interactions in the wake behind a stepped cylinder," Phys. Fluids **14**, 1548–1551 (2002).
[11]C. Morton and S. Yarusevych, "Vortex shedding in the wake of a step cylinder," Phys. Fluids **22**, 083602 (2010).
[12]C. Morton and S. Yarusevych, "Vortex dynamics in the turbulent wake of a single step cylinder," J. Fluids Eng. **136**(3), 031204 (2014).
[13]J. McClure, C. Morton, and S. Yarusevych, "Flow development and structural loading on dual step cylinders in laminar shedding regime," Phys. Fluids **27**, 063602 (2015).
[14]C. Tian, F. Jiang, B. Pettersen, and H. I. Andersson, "Numerical investigation of flow around a step cylinder," in *Proceedings of 9th National Conference on Computational Mechanics, Trondheim, Norway* (CIMNE, 2017), pp. 369–384.
[15]C. Tian, F. Jiang, B. Pettersen, and H. I. Andersson, "Antisymmetric vortex interactions in the wake behind a step cylinder," Phys. Fluids **29**, 101704 (2017).
[16]C. Tian, F. Jiang, B. Pettersen, and H. I. Andersson, "The long periodicity of vortex dislocations in the wake behind a step cylinder," in *Proceedings of 10th National Conference on Computational Mechanics, Trondheim, Norway* (CIMNE, 2019), pp. 81–99.
[17]C. Tian, F. Jiang, B. Pettersen, and H. I. Andersson, "Vortex dislocation mechanisms in the near wake of a step cylinder," J. Fluid Mech. **891**, A24 (2020).
[18]C. Ji, X. Yang, Y. Yu, Y. Cui, and N. Srinil, "Numerical simulations of flows around a dual step cylinder with different diameter ratios at low Reynolds number," Eur. J. Mech.: B/Fluids **79**, 332–344 (2020).
[19]J. Jeong and F. Hussain, "On the identification of a vortex," J. Fluid Mech. **285**, 69–94 (1995).
[20]M. Manhart, "A zonal grid algorithm for DNS of turbulent boundary layers," Comput. Fluids **33**, 435–461 (2004).
[21]J. H. Williamson, "Low-storage Runge-Kutta schemes," J. Comput. Phys. **35**, 48–56 (1980).
[22]H. L. Stone, "Iterative solution of implicit approximations of multidimensional partial differential equations," SIAM J. Numer. Anal. **5**, 530–558 (1968).
[23]F. Jiang, H. I. Andersson, J. P. Gallardo, and L. Okulov, "On the peculiar structure of a helical wake vortex behind an inclined prolate spheroid," J. Fluid Mech. **801**, 1–12 (2016).
[24]N. Peller, A. L. Duc, F. Tremblay, and M. Manhart, "High-order stable interpolations for immersed boundary methods," Int. J. Numer. Methods Fluids **52**, 1175–1193 (2006).
[25]C. Norberg, "Fluctuating lift on a circular cylinder: Review and new measurements," J. Fluids Struct. **17**, 57–96 (2003).
[26]C. H. K. Williamson and G. L. Brown, "A series in $1/\sqrt{\mathrm{Re}}$ to represent the Strouhal-Reynolds number relationship of the cylinder wake," J. Fluids Struct. **12**, 1073–1085 (1998).
[27]M. M. Zdravkovich, *Flow Around Circular Cylinders: Volume 1: Fundamentals* (Oxford University Press, 1997).
[28]M. Yagita, Y. Kojima, and K. Matsuzaki, "On vortex shedding from circular cylinder with step," Bull. JSME **27**, 426–431 (1984).